ENGINEERING MATERIALS:

METALS AND ALLOYS

SECOND EDITION

ZEISS
Seeing beyond

WILEY

Imprint

Boschstr. 12, 69469 Weinheim,
Germany
Email: info@wiley-vch.de

Carl Zeiss Microscopy GmbH
Carl-Zeiss-Promenade 10,
07745 Jena,
Germany
www.zeiss.com/microscopy

Editor-in-Chief:
Dr. Christene A. Smith

Senior Account Manager:
Dr. Stefanie Krauth

Cover image: Two examples for the characterization of crystal orientation from the micro- to the nanoscale using multiple microscopic modalities. Highly deformed stain-less steel investigated with a ZEISS scanning electron microscope using channeling contrast imaging to visualize dislocation networks and strong crystalline orientation changes within the grains, image width 34 µm (grey-scale image). 3D grain map of a metal alloy, an Al-4wt%Cu sample with gauge section dimension of 1.25 mm length, 1.0 mm width and 0.5 mm thickness. Sample scanned using Lab based Diffraction Contrast Tomography (LabDCT) in a ZEISS X-ray microscope (inset, colored image).

Editorial

From the dawn of early civilizations, the discovery of metals has played a pivotal role in shaping the course of human history, creating new revolutions along the way. Metals have played a foundational role in human development right from the creation of early metal tools and weapons to advancement of agriculture, construction and transport – ultimately forging the path to today's modern society. Each era, starting with the Gold, Bronze and Iron Ages, advanced our fundamental knowledge and has led us to discovering newer alloys along with innovative techniques to produce stronger and more customized materials. By the mid-20th century, all of the metals in the sub-transuranic periodic table had been discovered and several of their alloys with increasingly remarkable properties had been created.

However, prominent breakthroughs in the field of metallurgy and materials science began when early researchers started investigating why metals and alloys fail in certain ways. The pursuit of understanding materials to make them stronger, lighter and more reliable, unravelled the fact that there is a deep-rooted connection between the microstructure, properties, processing and performance of any given material. In parallel to the materials discoveries taking place, significant scientific breakthroughs in imaging using light, electron and X-rays paved the way for characterizing materials down to their atomic arrangements and enabling the study of materials in ways never before possible; **microscopy would soon become the centrepiece of materials science.**

More recently, with the synergies of technologies such as machine learning and advanced manufacturing methods such as 3D additive manufacturing, far more complex materials can be explored. Today's metals research is propelled by the requirement to adapt the world to a low carbon economy, free of fossil fuel pollution. This paradigm shift requires stronger, lighter and more durable alloys and advanced steels to lead us into the middle of the 21st century and beyond.

This booklet aims to give you an overview of recent achievements in engineering materials research. A brief introduction details some advanced microscopy techniques from ZEISS and their specific benefits for your research. This is followed by a selection of peer-reviewed articles from various Wiley journals, condensed into a digestible format with links to the original article DOIs.

In a concluding interview, Dr Kaoru Sato from JFE-Techno-Research Corporation shares his views on current challenges and future developments in microscopy applications for engineering materials, particularly in metals and alloys.

Dr Hrishikesh Bale
Market Solutions Manager
ZEISS Research Microscopy Solutions

Contents

Introduction

New stronger, tough, durable, lightweight and fracture-resistant materials open doors to new technologies, whether it is in the applications of high-speed air or ground transportation, long lasting and economical construction, safe nuclear installation, or more advanced space exploration technologies. Designing and developing the engineering materials for tomorrow's innovation challenges demands an ever-better understanding of the complex connections between processing, properties and the underlying structures that, collectively, influence how a material performs and why it might fail.

The demands for materials to meet a variety of structural needs has spawned advancements in an assortment of fields including advanced alloys with exceptional corrosion resistance, high temperature performance, fatigue and fracture resistance and high strength-to-weight ratio composite structures.

Developing and improving these types of engineering materials takes a detailed understanding of the connections between processing, structure, performance and properties throughout the material's life cycle. This is even more important as advanced technologies such as additive manufacturing become increasingly prolific and more complex. Microscopy characterization techniques are central to this paradigm, enabling observation of the microstructure of any given material revealing its grain structure, crystallographic texture, phases and phase transitions, inclusion and impurity distributions, and surface finish.

Among all of the engineering materials classes, metals and alloys present the widest range of properties that can be highly tailored through processing as per the applications needs, for example strength, hardness, malleability, good electrical and thermal conductivity, and corrosion resistance. Commercial metal alloys attempt to combine beneficial mechanical, electrical or chemical properties in order to create metals more useful for particular applications than any of their component elements. Some of the key characteristics of metals that make them an attractive and sought after engineering material are the ease of production, availability, scalability in production, recyclability and most importantly the ability to control properties through processing and microstructure control.

In contrast to traditional development approaches in metals and alloys, present day research engages significantly in engineer-

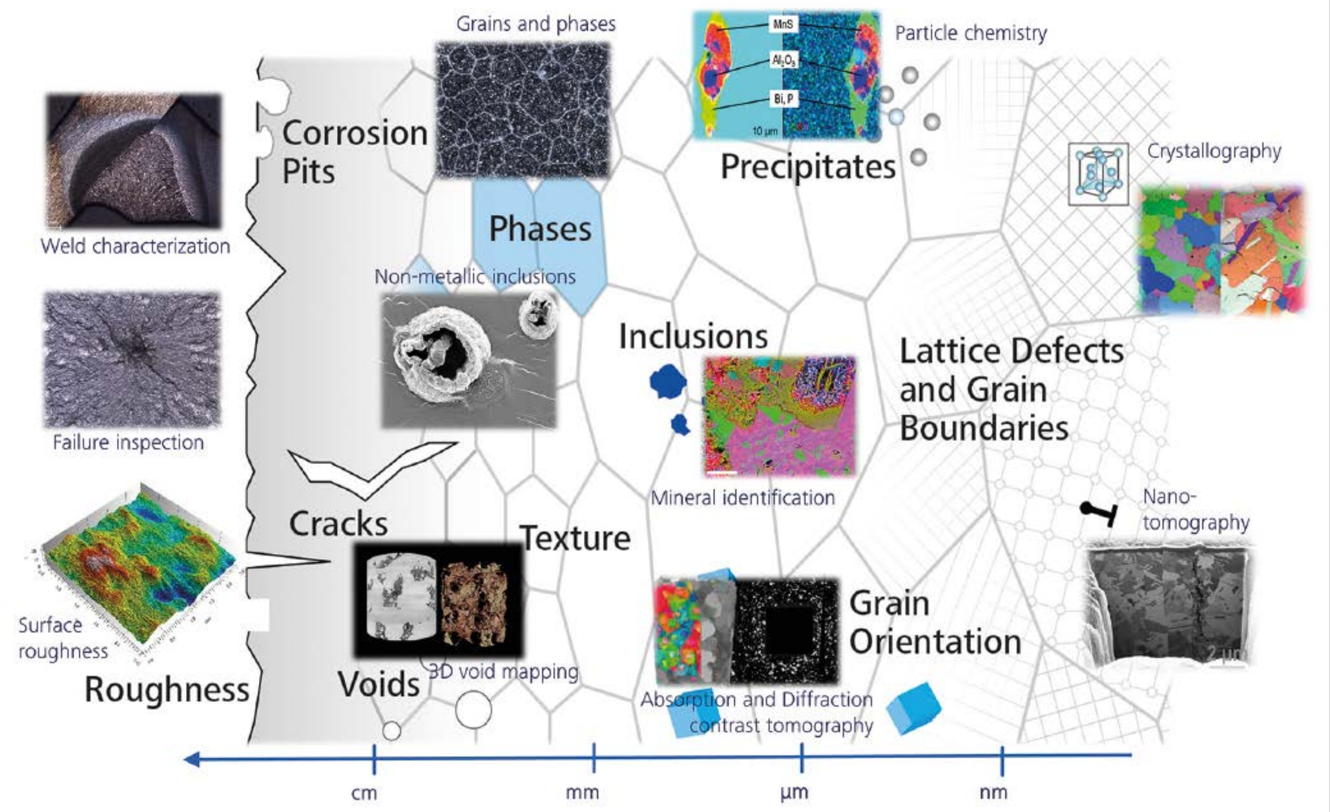

Fig. 1: *Overview of metals.*

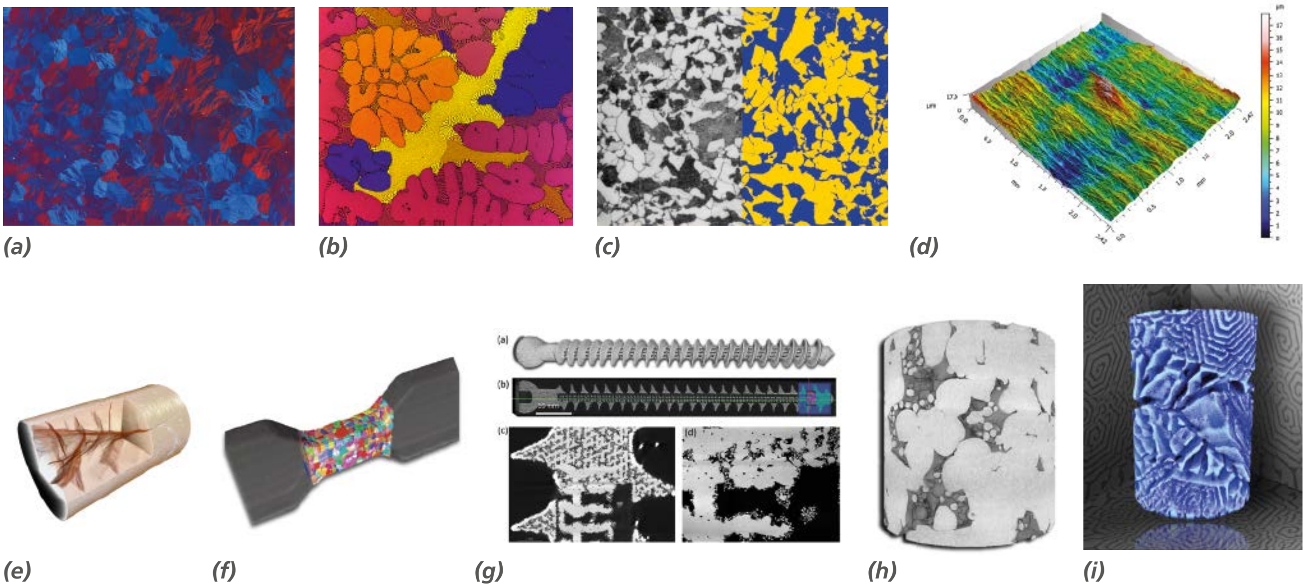
(a) (b) (c) (d)

(e) (f) (g) (h) (i)

Fig. 2: (a) Light microscopy image of a pure magnesium sample using polarization contrast shows the structural anisotropy; (b) polarization contrast light microscopy image from a Barker etched anodized AlNi3.5 sample; (c) ferrite and pearlite phase in steel imaged using light microscopy and quantitatively analyzed; (d) laser polished surface of stainless steel test piece. 3D view of colour-coded height map shows surface texture of areas with different process parameters; (e) non-destructive 3D rendering of crack networks formed due to corrosion fatigue in the shank section of a load-bearing steel bolt (XRM); (f) 3D grain map of an Al-4wt%Cu sample with gauge section dimension of (length) 1.25 mm, (width) 1.0 mm and (thickness) 0.5 mm. Sample scanned using Lab based Diffraction Contrast Tomography (LabDCT); (g) volumetric rendering of a 3D printed Ti-6Al-4V screw (top). Blue dotted line indicates cross-sectional view from a region of interest scan, (bottom) reveals local microstructure and defects such voids and unsintered powder particles; (h) 3D volumetric rendering of sintered CoCr particles. The consolidated bulk after sintering and portions of unsintered powder can be observed; (i) 3D rendering of a reconstructed nanoscale X-ray tomography dataset obtained from a Zn–Mg spiral eutectic sample.

ing the microstructure in order to enhance mechanical, thermal and electrical properties. Using data-guided precise control of the grain size, engineering the grain boundaries and distribution of precipitates and controlling the presence of inclusions, voids and other defects, remarkable improvements in the properties of traditional metals and alloys can be achieved. At the heart of engineering such complex materials lie material characterization techniques.

As shown in Figure 1, the microstructure of any metal or alloy encompasses diverse features ranging from surface roughness, pits and cracks; grain characteristics (size, crystallographic orientation and morphology), texture, twinning, voids, inclusions and precipitates at the 10–100 µm range; and ultimately nanoscale features such as dislocations, nano-precipitates, lattice defects, crack initiation sites and nano-crystalline grain features. Such a detailed microstructural evaluation drives the need to include several microscopy techniques providing different imaging modalities, each revealing uniquely important pieces of information. The mechanisms that individually contribute to strength, toughness and other important properties can originate from very different length scales in a material's structural architecture and it is very important to capture their interplay in their native state. This has led to the emergence of correlative microscopy approaches that combine information gathered from various modalities at different length scales, enabling researchers to gather comprehensive information for a given material system.

Understanding impact of macroscale features on material properties and performance

At the macroscale, materials insights related to geometric defects, surface roughness, cracks, voids and inclusions can be characterized effectively using light and X-ray microscopy methods (Figure 2). Through a variety of modes including brightfield, darkfield and polarization contrast, light microscopy can generate a wealth of information readily on metals samples. While light microscopy provides rapid information from the surface over a wide area, X-ray methods enable peering into the sub-surface non-destructively delivering three-dimensional (3D) information on complex microstructural features such as crack networks, void distributions, etc. With advances in diffraction contrast tomography, 3D crystallographic grain characterization is now possible. This non-destructively delivers information on grain size, morphology and orientations, which provides an early macroscale overview of the sample before needing further high resolution insights from some of the electron microscopy techniques. With its ability to capture the microstructural information in 3D in a single snapshot, X-ray microscopy methods are particularly best suited for new-age manufacturing methods such as 3D printing where structural parts with an ever increasing material and structural complexity are being produced. Recent advances in

X-ray microscopy now enable 3D nanoscale microstructural characterization, providing information on nanoprecipitates, eutectic microstructures, etc.

Comprehensive characterization from micro- to nanoscale

Electron microscopy techniques have become an integral part of materials characterization workflow and to many researchers the scanning electron microscope (SEM) is the go-to 'Swiss-knife' among all of the characterization techniques. SEM provides a unique opportunity for characterizing materials from micron to sub-nanometer scale, through a variety of imaging modalities, all on a single imaging platform. Offering the flexibility to augment imaging with a wide-ranging detector probe landscape, an SEM instrument readily delivers critical information related to chemical makeup, crystallographic microstructure (Figure 3) and phase identification. Within the area of metals and alloys analysis, an SEM can quickly deliver qualitative as well as quantitative information on inclusions, precipitates and other morphological features. Advanced detector technology with improved secondary and backscattered electron imaging performance, along with highly refined electron beam column designs, supports combining information from multiple detectors, delivering exceptional contrast that can discern crystal defects, crystal orientations, and subgrain information such as twinning and slip band formations (Figures 4 and 5).

Surface characterization of fracture at high resolution delivers information necessary for the determination of the fracture mode and in the analysis of crack propagation, successively enables researchers to study the relationship between microstructure and fracture resistance. These methodologies are an integral part of the root cause analysis workflows used to study structural failures of critical parts used in engineering applications. Furthermore, these imaging modalities can also be combined with *in situ* imaging for microstructure characterization during deformation.

A gamut of modalities to assess grain characteristics and deformation behaviour

In addition to the core modality of electron backscattered imaging, additional probes enable other important measurements that are highly essential to metals and alloys research. Energy dispersive X-ray spectros-

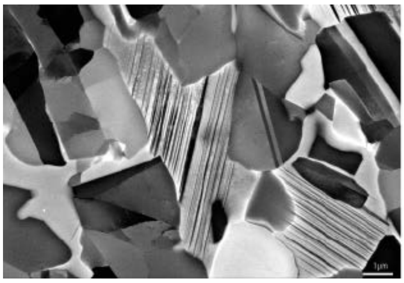

Fig. 3: Scanning electron microscopy (SEM) delivers extremely high contrast of crystal orientations and defects in the high temperature alloy $TiAl_2$. $TiAl_2$ is an alloy of intermetallic compounds with lower density and superior oxidation resistance. The image is taken with the AsB detector at 15 kV. The presence of crystal defects and the preferential crystalline orientations observed in such images may be correlated with improved desired mechanical properties.

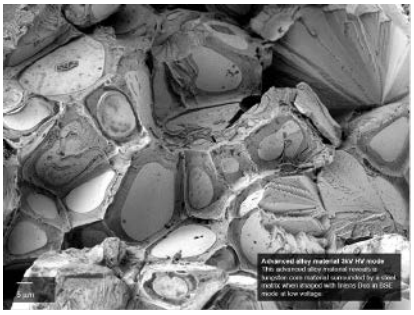

***Fig. 4:** Advanced alloy material imaged at 3kV in HV mode. This advanced alloy material reveals a tungsten core material surrounded by a steel matrix when imaged with Inlens Duo in BSE mode at low voltage.*

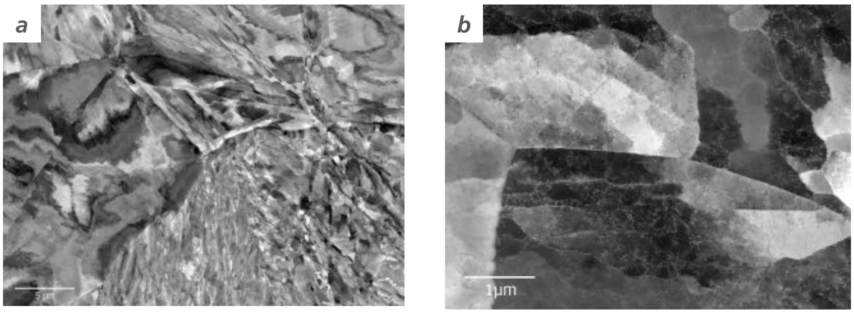

***Fig. 5:** Channeling contrast imaging of dislocation networks in highly deformed stainless steel. The sample is imaged at 30 kV electron beam energy. (a) Strong crystalline orientation changes within the grains. (b) Dislocation networks formed by the deformation.*

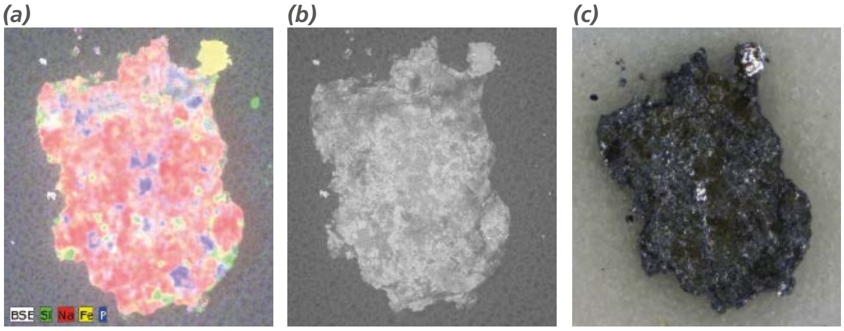

***Fig. 6:** Particulate contamination is an important aspect of technical cleanliness. Multi-modal SEM imaging of a contamination particulate provides: (a) elemental composition though EDS mapping, (b) and (c) morphological details through backscattered electron microscopy and light microscopy, respectively.*

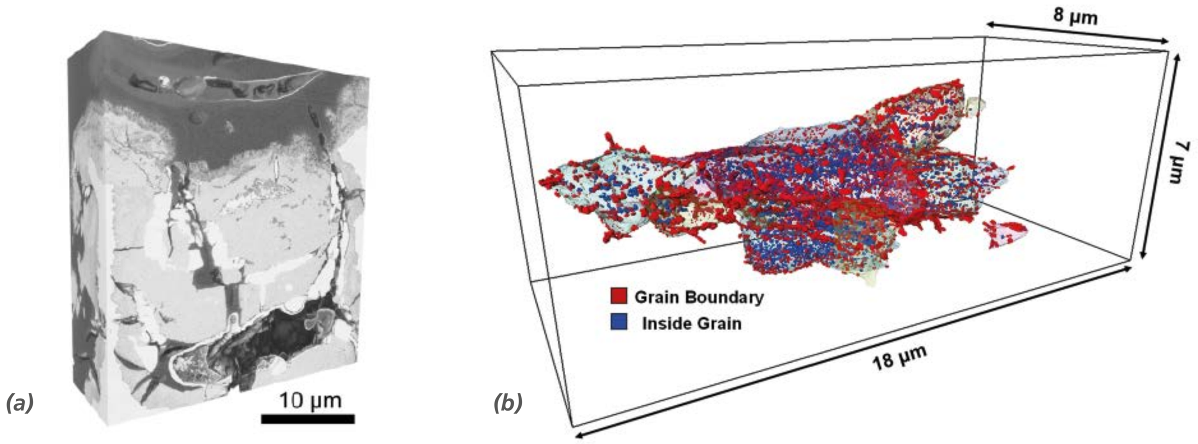

Fig. 7: *(a) High resolution serial section FIB-SEM tomography (8 nm/voxel) from a correlative microscopy experiment to study the process of intergranular corrosion observed in a magnesium alloy. Sample courtesy of the University of Manchester; (b) 3D FIB-SEM tomography data on the precipitate distribution in aluminum 7075 alloy. The 3D data provides quantitative information on the spatial distribution of precipitates with respect to the grain boundaries. Sample courtesy of Prof. N. Chawla, Purdue University.*

copy (EDS) enables a highly detailed and correlated chemical analysis of precipitates and inclusions (Figure 6). Understanding of the chemical makeup and distribution of the inclusions and precipitates enables metallurgists to modify the materials processing route and chemistries and fine tune the properties and performance of a metal or alloy system.

The electron backscattered diffraction (EBSD) technique brings an exceptional capability to electron microscopy by allowing the measurement of grain size, crystallographic orientation, texture, and grain boundary character distribution with a sufficiently high resolution down to 10 nm. EBSD enables material characterization at different length scales providing information on a number of key microstructural characteristics. Since the mechanical properties of metals and alloys are strongly coupled to several microstructural aspects such as the size, shape, and distribution of grains, the presence of texture, grain boundary character, and also the grain boundary plane distribution, EBSD is one of the prime characterization methods used in the study of metals and alloys.

The knowledge of the distribution of lattice defects such as dislocations and stacking faults within grains and their location with respect to grain boundaries and orientations offers key insights into the deformation behaviour and fracture properties of metals and alloys. Electron channelling contrast imaging (ECCI) is the adaptation of scanning electron microscopy to directly observe the lattice defects quantitatively using electron channelling along crystal planes. The technique can also be combined with *in situ* deformation of metals samples to make direct observations of the formation of dislocation networks under the influence of mechanical loads and elevated temperatures.

Precise, high-throughput cross-sectioning for high-resolution sub-surface microstructural characterization

Site-specific characterization using a suitable probing modality is extremely important in order to isolate and understand many of the underlying mechanisms that operate at the microstructural length scale. The first step in such a study is to precisely target a feature of interest, for example, a unique void feature, a precipitate located along a certain grain boundary or a specific grain boundary with unique boundary surface characteristics. Focused ion beams (FIB) offer the excellent capability of precise sectioning to reveal the sub-surface features, while maintaining a virtually deformation free microstructure. Thin serial sectioning using FIB milling combined with standard live SEM imaging (Figure 7) or a combination of EDS or EBSD imaging (Figure 8) enables high resolution multichannel 3D tomography focusing on specific sub-surface sites. This facilitates the investigation of grain boundary interactions with precipitates, influence of grain orientation and grain boundary surface on the material properties such as fracture toughness, corrosion, thermal and electrical properties in metals and alloys. More recently even more massive material removal, at least three orders of magnitude more than traditional FIB milling has been made possible by incorporating femto-second lasers on the FIB-SEMs. This new rapid milling capability enables high throughput characterization of larger sample areas or deeper regions of interest (Figure 8).

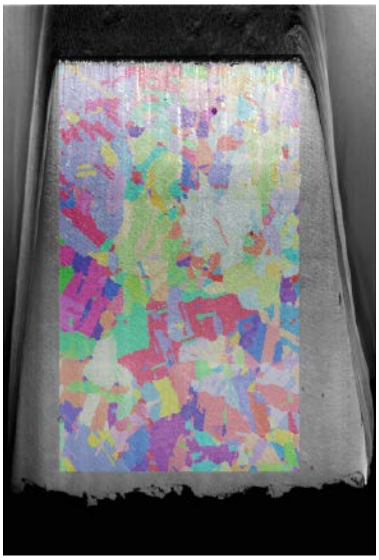

Fig. 8: *Laser-polished sample surfaces produce satisfactory EBSD grain maps without the need for Ga-FIB polishing steps in cases where a quick overview of a large area of the sample is sufficient. For deeper analysis and high resolution grain maps, a region of interest can be selected from the overview EBSD maps and used to run high resolution grain mapping after gallium polishing.*

Enhancing Ductility and Fatigue Strength of Additively Manufactured Metallic Materials by Preheating the Build Platform

Adapted from P.D. Nezhadfar, *et al.*, 2020

This study investigates the effect of preheating the build platform on the tensile and fatigue behavior of 316L stainless steel, fused using a laser beam powder bed. It was found that this process modification causes fewer and smaller volumetric defects in the manufactured pieces.

Introduction

Additive manufacturing (AM) involves rapid melting and solidification, creating defects like gas-entrapped pores and lack of fusion (LoF), along with residual stresses and microstructure variations. These issues impact material fatigue resistance [1], influenced by the thermal history experienced by the piece throughout the fabrication process and factors such as piece size, geometry, interlayer time, building environment, and process parameters [2–4].

Altering the AM process's thermal history includes preheating the build platform, which significantly influences the material's final structure and reduces tensile anisotropy. While some studies have explored preheating's impact on residual stresses and grain structure [5,6], its effects on fatigue performance remain unexamined. This study aims to assess how preheating the build platform affects both the microstructure and the mechanical properties, especially the fatigue resistance of laser beam powder bed fused (LB-PBF) metallic materials.

Materials and methods

316L stainless steel powder was used to fabricate two sets of cylindrical bars and net-shaped tensile test specimens. One set was made without preheating the build platform (no preheat, NP), while in the other the build platform was preheated to 150°C (P150). Process parameters included laser power 200 W, hatching distance 0.11 mm, scan speed 1833.3 mm/s, and layer thickness 0.05 mm. The cylindrical bars were machined into round fatigue specimens with straight gauge sections.

Specimens were cross-sectioned perpendicular to the final laser track on the top layer. Melt pool boundaries were then revealed on the longitudinal plane parallel to the build direction through chemical etching. X-ray computed tomography (CT) scans using a Zeiss Xradia 620 system allowed 3D visualization and comparison of porosity levels in each condition (NP and P150). Electron backscatter diffraction (EBSD) scanning on mirror-finished polished longitudinal cross sections was conducted using a Zeiss Crossbeam 550 SEM/FIB for microstructure characterization.

Quasi-static tensile and fully reversed, strain-controlled fatigue tests were conducted using an MTS Landmark servohydraulic load frame equipped with a 100-kN load cell. Tensile tests were performed at 0.001 s^{-1} at room temperature in two steps: initially up to 0.045 mm/mm of strain with an extensometer mounted on the specimen to measure strain. Subsequently, the extensometer was removed, and the test continued in displacement-controlled mode until fracture occurred. Fully reversed, strain-controlled fatigue tests were conducted over strain amplitudes ranging from 0.00175 to 0.0040 mm/mm to encompass the material's cyclic behavior from low cycle fatigue (LCF) to high cycle fatigue (HCF) regimes. Test frequencies were adjusted for each strain level to achieve an average cyclic strain rate of approximately 0.02 s^{-1}.

Results and discussion

Microstructure characterization

The melt pools are shallower in the NP condition (90 µm) compared to the P150 condition (150 µm). Melt pool and overlap depths, denoted as d_p and d_o respectively, influence the formation of volumetric defects [7,8]. These parameters, normalized

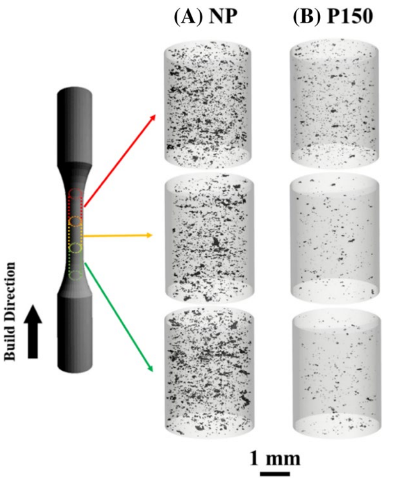

Figure 1. *X-ray CT scan results throughout the gage section of LB-PBF 316L SS specimens from (A) NP and (B) P150 conditions.*

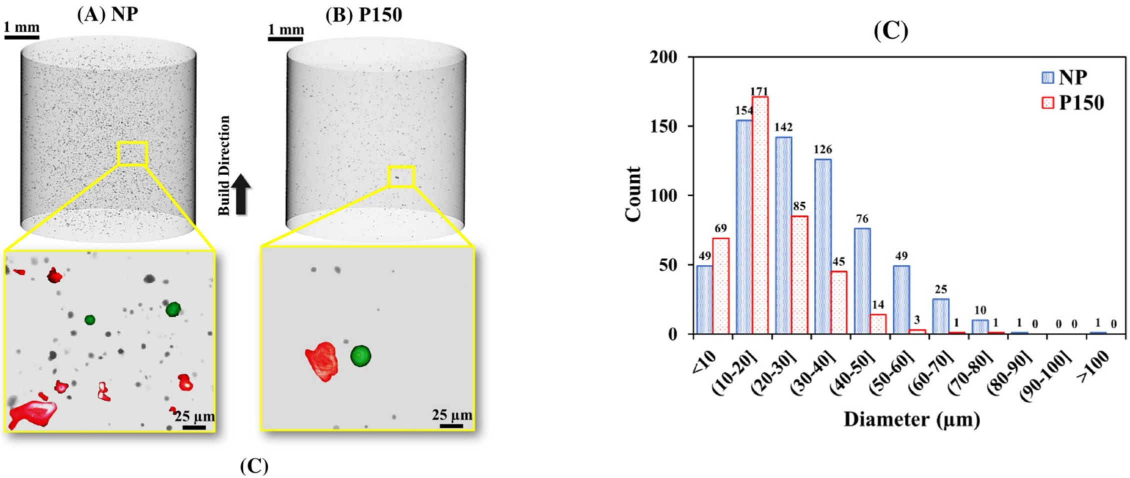

Figure 2. *X-ray CT scan results from a small section (~5 mm) of the gage section of machined LB-PBF 316L SS specimens for (A) NP and (B) P150 conditions, as well as (C) defects size distributions based on 100 radial cross-sections.*

by the layer thickness *t*, help evaluate the probability of volumetric defect formation. The d_p/t and d_o/t ratios for the NP condition were found to be 1.8 and 1.3 respectively, which are lower than those of the P150 condition (3 and 1.85, respectively). Deeper melt pools and lower cooling/solidification rates provide sufficient overlap depth and more time for gas-entrapped pores to escape from the melt pool during solidification in the P150 condition.

In Figure 1 it can be seen that preheating the build platform decreases the size and population of the defects throughout the gage section as compared with the NP condition. Moreover, some examples of LoF defects and gas-entrapped pores are highlighted in Figure 2A,B by red and green, respectively. The diameter of the defects was statistically compared in Figure 2C. These results prove that the P150 specimens contain fewer and smaller volumetric defects as compared with the NP specimens.

The cellular structure for both studied conditions are shown in Figure 3; the cells are more equiaxed and appear finer in the P150 condition (Figure 3B) compared to the NP condition (Figure 3A). This can be explained by the lower temperature gradient and consequently slower cooling/solidification rates for P150. Moreover, preheating the build platform may lead to recrystallization of the grains; subgrains are formed in the P150 condition (indicated by yellow dashed arrows/boundaries in Figure 3B). However, these subgrains do not transform into grains with high-angle boundaries to result in grain refinement, with an average grain size of 16 µm, which was calculated for both NP and P150 conditions using EBSD results. This may be due to the preheating temperature being insufficient to provide the necessary driving force energy for recrystallization of the grains.

Quasi-static tensile behavior

Preheating the build platform increased ductility by about 18% without compromising the strength of the material. Improved ductility may be associated with fewer volumetric defects in the P150 specimens (Figure 2) and grain orientation along the FCC preferred slip system.

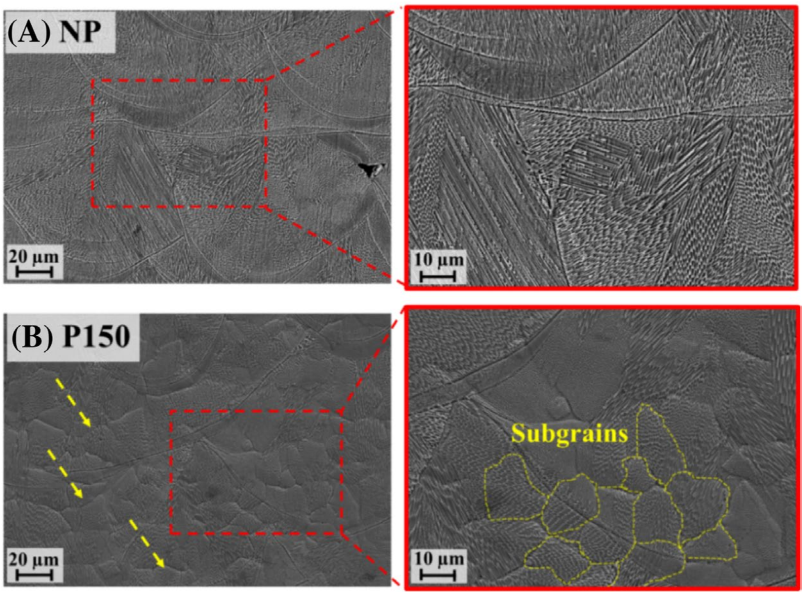

Figure 3. *Microstructure characterization of LB-PBF 316L SS fabricated in (A) NP and (B) P150 conditions showing the cellular structures.*

In line with the X-ray CT results, the tensile fracture surface of NP specimens showed a higher level of volumetric defects compared to that of their P150 counterparts, which could have contributed to the lower ductility observed. Additionally, a finer cellular structure is noticeable on the fracture surface of the P150 specimen.

Fatigue behavior

Preheating the build platform had no effect on cyclic deformation, as NP and P150 specimens exhibited similar cyclic deformation behaviors: initial cyclic hardening followed by cyclic softening. Additionally, the stable stress–strain hysteresis loops were identical for both conditions.

There is some improvement in the fatigue performance of LB-PBF 316L SS across life regimes by preheating the build platform up to 150°C, most likely due to lower volumetric defects, specifically LoF ones. The longer fatigue lives for P150 specimens in the HCF regime are attributed to fewer and smaller volumetric defects compared to NP specimens (Figure 2).

Conclusions

It was found that preheating the build platform lowered the cooling and solidification rates, which resulted in deeper melt pools and overlap depths, leading to fewer and smaller volumetric defects. Consequently, the total elongation to failure of P150 LB-PBF 316L SS under quasi-static tensile loading increased by about 18% compared to the NP condition. Finally, it is concluded that preheating the build platform significantly enhanced the fatigue resistance of LB-PBF 316L SS across all life regimes investigated in this study.

Copyright: 10.1111/ffe.13372
P.D. Nezhadfar, N. Shamsaei, N. Phan
Fatigue & Fracture of Engineering Materials
& Structures

References

[1] Yadollahi, A. and Shamsaei, N. (2017). Additive manufacturing of fatigue resistant materials: Challenges and opportunities. *International Journal of Fatigue*. DOI: 10.1016/J.IJFATIGUE.2017.01.001.

[2] Yadollahi, A. *et al*. (2015). Effects of process time interval and heat treatment on the mechanical and microstructural properties of direct laser deposited 316L stainless steel. *Materials Science and Engineering: A*. DOI: 10.1016/J.MSEA.2015.07.056.

[3] Nezhadfar, P.D. *et al*. (2020). Improved high cycle fatigue performance of additively manufactured 17-4 PH stainless steel via in-process refining micro-/defect-structure. *Additive Manufacturing*. DOI: 10.1016/J.ADDMA.2020.101604.

[4] Averyanova, M. *et al*. (2012). Experimental design approach to optimize selective laser melting of martensitic 17-4 PH powder: Part i - Single laser tracks and first layer. *Rapid Prototyping Journal*. DOI: 10.1108/13552541211193476/FULL/XML.

[5] Li, W. *et al*. (2016). Effect of substrate preheating on the texture, phase and nanohardness of a Ti–45Al–2Cr–5Nb alloy processed by selective laser melting. *Scripta Materialia*. DOI: 10.1016/J.SCRIPTAMAT.2016.02.022.

[6] Leung, C.L.A. *et al*. (2019). Effect of preheating on the thermal, microstructural and mechanical properties of selective electron beam melted Ti-6Al-4V components. *Materials & Design*. DOI: 10.1016/J.MATDES.2019.107792.

[7] Tang, M. *et al*. (2017). Prediction of lack-of-fusion porosity for powder bed fusion. *Additive Manufacturing*. DOI: 10.1016/J.ADDMA.2016.12.001.

[8] Scime, L. and Beuth, J. (2019). Melt pool geometry and morphology variability for the Inconel 718 alloy in a laser powder bed fusion additive manufacturing process. *Additive Manufacturing*. DOI: 10.1016/J.ADDMA.2019.100830.

Correlative Analysis of Microstructural and Magnetic Characteristics of Dual-Phase High-Carbon Steel

Adapted from N. Sarmadi, *et al.*, 2023

This study investigates how compressive and controlled-thermal deformation affects high-carbon steel to create a dual-phase microstructure. It establishes an empirical link between these phases and magnetic properties, offering a non-destructive assessment method for dual-phase low-alloyed high-carbon steels.

Introduction

Dual-phase (DP) high-carbon steels (HCS) are prized for their exceptional hardness, strength, toughness, and wear resistance, making them a mainstay in high-strength steel classes. Typically, these steels exhibit an austenite-martensitic microstructure, where the combination of soft matrix and hard martensite particles dictates mechanical properties, including strength and ductility [1,2]. Tailoring the microstructure's constituents—type, volume fraction, size, morphology, and spatial distribution—allows for customization of desired mechanical and magnetic properties in DP steels [3,4].

Quantifying steel microstructure is typically complex, time-consuming, and costly. Thus, exploring unconventional non-destructive testing, particularly through magnetic property assessment, is valuable. Different steel microstructural phases—like austenite, bainite, ferrite, and martensite—exhibit distinct magnetic properties. Leveraging the link between microstructural changes and magnetic characteristics enables accurate prediction of the steel properties [5]. While many studies have examined magnetic properties in low-carbon steels, few have investigated this relationship in low-alloyed HCSs [6,7].

In this context, vibrating-sample magnetometry (VSM) measures magnetic properties in diverse samples, including steels. Combining the heightened sensitivity of SQUID (superconducting quantum interference device) magnetometry with VSM's rapid results enables the collection of significantly more data in a shorter time span.

Experimental Section

The study utilized cylindrical samples (15x5 mm) of industrial-grade HCS with a chemical composition of 1.0%C-0.2%-Si-1.0%Mn-0.6%Cr (in wt%). Samples underwent compression at room temperature using an Instron 5982 electromechanical testing instrument. Metastable retained austenite (RA) phases transformed to martensite due to the transformation-induced plasticity (TRIP) effect [8,9]. Each compressed sample exhibited varying RA and martensite fractions influenced by factors like surface morphology, chemical composition, alloying elements, and austenite fault energy [10].

HCS samples were mirror polished and subjected to different heat treatments, including heating to 1100°C in an IR furnace with confocal microscopy for in-situ observations in Ar atmosphere for 7 minutes. Cooling rates of 200, 400, and 600°C min-1 (in He atmosphere) were applied for one-stage treatment, while two-stage treatment included interrupted cooling after the same heating and soaking conditions. Microstructural characterization followed X-ray diffraction, meeting bulk solid analysis standards.

Microscopic examination of transformed austenite and martensite relied on unit cell orientation. Electron back-scattered diffraction (EBSD) using an Oxford system attached to a Carl Zeiss AURIGA Cross-Beam FEG-SEM workstation at 20 kV was employed. EBSD patterns were collected at a binning mode of 2 x 2 and scanning step size of 0.15 µm using AZTEC software to generate Kernel average misorientation (KAM) maps displaying misorientation levels with assorted colors.

The magnetic properties (saturation magnetization, remanence, and coercivity) of 1 mm x 5 mm samples were evaluated using a sensitive SQUID Quantum Design MPMS-3 magnetometer equipped with VSM. A correlation was established between saturation magnetization (MS) and the retained austenite (VRA) fraction in compressed samples.

Results and Discussion

XRD patterns revealed a notable decrease in V_{RA} during compression tests from 20 kN to 69.87 kN at room temperature. V_{RA} decreased from 17.4% in uncompressed samples to around 16.3% at 20 kN and further dropped sharply with higher loads. Microstructure analysis of HCS samples before and after compression (40 and 60 kN) displayed noticeable changes in residual austenite with increasing compression force (Figure 1). Martensitic structures, including plate and lath martensites, were

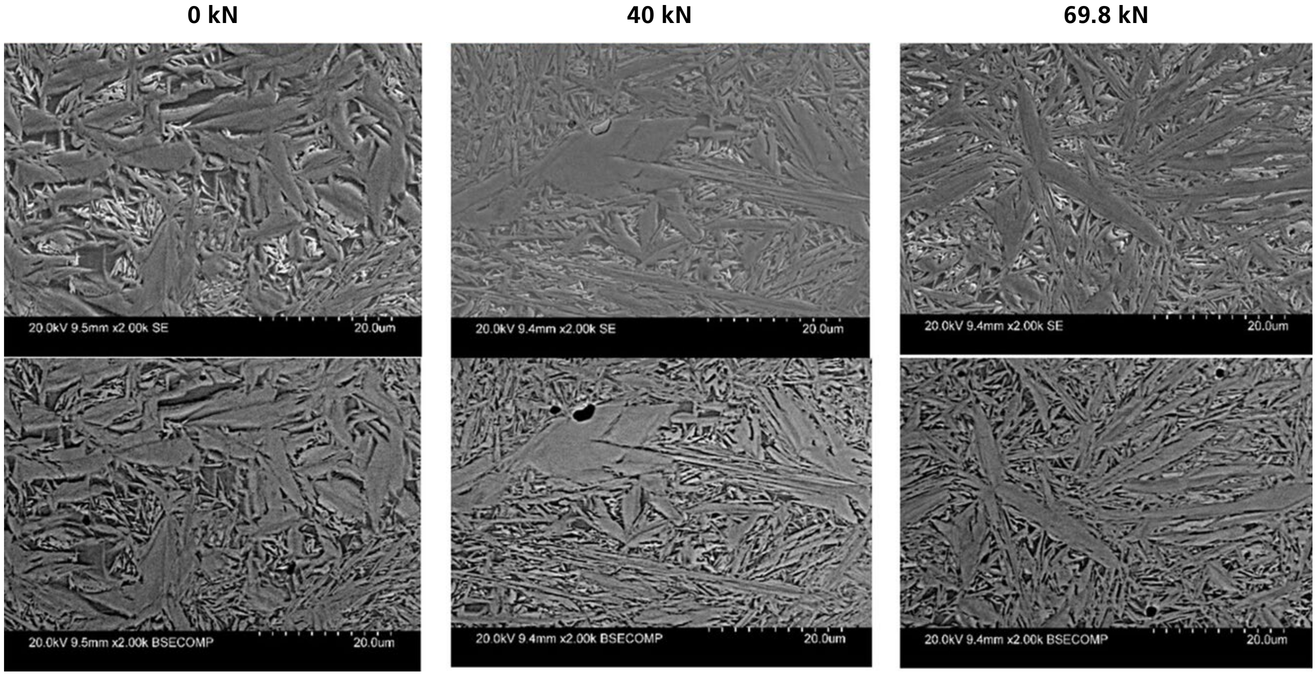
0 kN

40 kN

69.8 kN

Figure 1. *Scanning electron micrographs of samples subjected to different magnitudes of compression.*

observed, with a refined structure and dominant lath morphology at higher compressive forces. EBSD investigations indicated martensite dominance over retained austenite in both as received and 69.8 kN compressed samples, with significantly reduced austenite distribution suggesting transformation under compressive stress.

From EBSD data (Figure 2), local grain misorientation (KAM measures) were derived, providing insight into grain deformation [5]. The *n*th KAM at a point represents its average misorientation with *'n'* nearest neighbors, disregarding those above a set threshold. Martensite regions exhibit high misorientations (green), while RA regions display lower values (blue). Elevated KAM values around plate martensite boundaries (red) indicate greater deformation. Comparing misorientation indices between uncompressed and compressed samples reveals a shift to higher ranges in the compressed ones, indicating severe deformation and increased dislocation densities at austenitic-martensitic boundaries, corroborating XRD findings. Two methods were employed to produce DP steel in HCS samples: rapid cooling (He-quenching) and a dual-state heat treatment with interrupted cooling, primarily to preserve austenite before complete transformation to martensite.

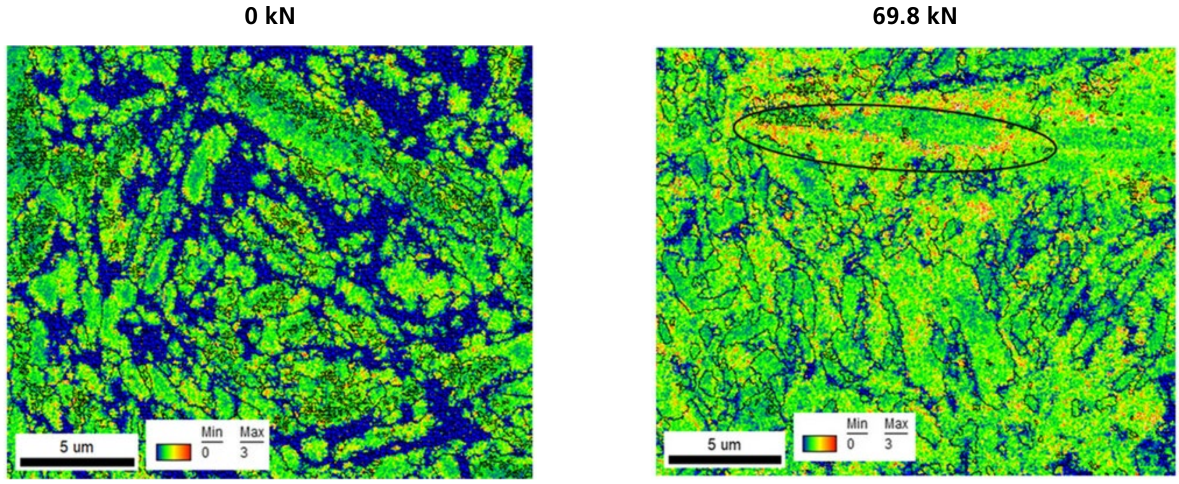
0 kN

69.8 kN

Figure 2. *KAM mapping of HCS samples under 0 and 69.8 kN compression.*

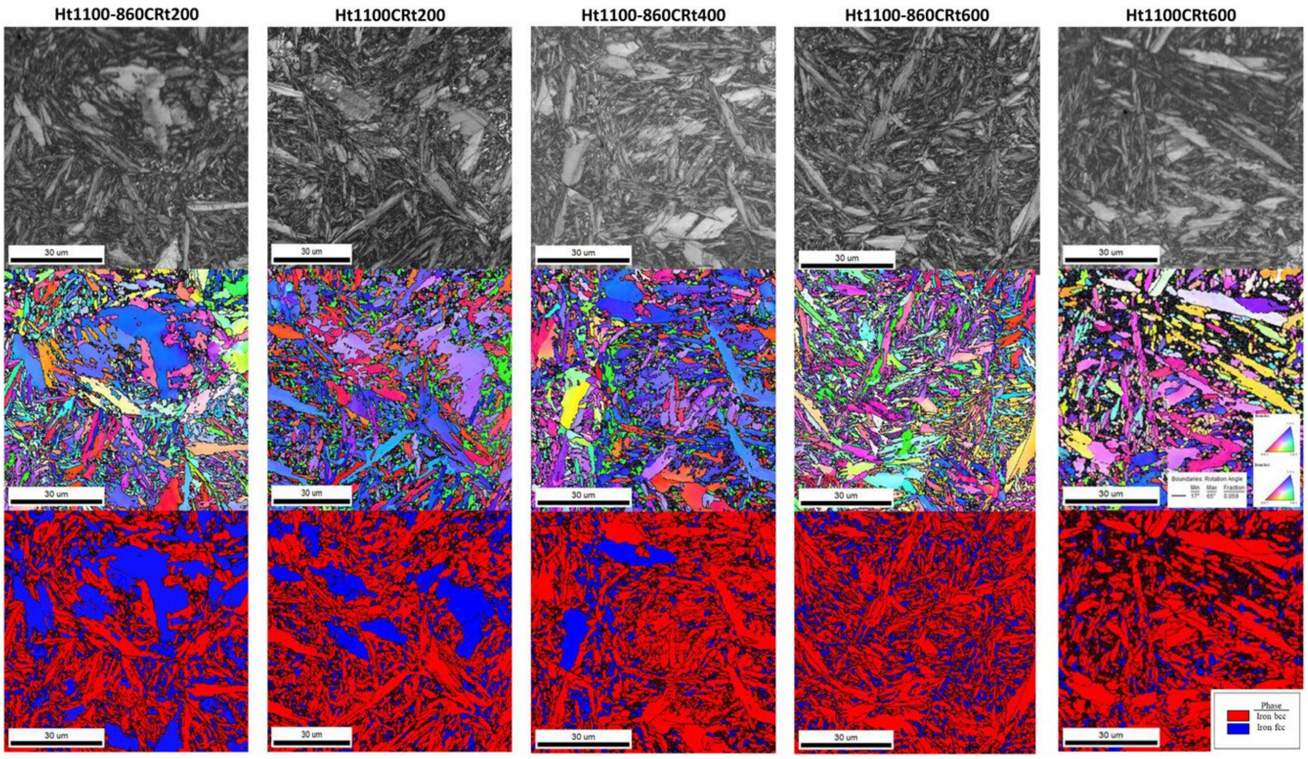

Figure 3. *EBSD analyses of HCS samples for different heat treatment conditions.*

Figure 3 illustrates EBSD micrographs, inverse pole figure maps, and phase maps of heat-treated samples. Interrupted cooling and two-stage heating led to a greater distribution of RA phases. Increasing cooling rates resulted in more martensite, with blockier grains at lower rates and finer structures at higher rates (600°C min^{-1}). Uninterrupted cooling samples also showed increased martensite with higher cooling rates. Notably, denser dislocation pileups were observed at martensite-austenite grain boundaries in uninterrupted samples cooled at 600°C min^{-1}.

Magnetic Characterization

The study finds that steel with complex microstructures has higher magnetic permeability due to domain wall pinning, unlike those with single-phase microstructures. Pinning sites trap domain walls, requiring an external field for release. In compressed samples, curves were closely grouped at various pressure ranges. Similarly, heat-treated samples cooled at the same rates, exhibited paired magnetization curves, reflecting comparable ferromagnetic behavior.

Saturation magnetization measurements showed that the most compressed sample had the highest saturation magnetization but the lowest coercivity and remanence. Heat-treated samples displayed consistent saturation magnetization trends corresponding to martensite content. However, coercivity and remanence exhibited contrasting trends with martensite content, influenced by factors such as internal stress, inclusions, dislocations, grain size, shape anisotropy, and interparticle interactions [11].

Based on the findings consolidated from studies on different steels, the order of saturation magnetization among steel microstructural phases is α^0 (BCT martensite) > α (BCC-ferrite and martensite) > ε (martensite) > γ (austenite) [12]. A correlation was established between saturation magnetization values of compressed samples and the volume fraction of the RA phase, using a polynomial equation fit to the data. This allows determination of austenite volume fraction from simple non-destructive magnetic tests. Validating with literature samples (WQ- fully martensitic) indicated partial extrapolation validity [13], likely influenced by sample preparation, RA: M ratio, grain size differences, residual stresses, etc.

Conclusion

The quantification of austenite and martensite phases in the HCS samples was investigated and the dependency of saturation magnetization on the volume fraction of ferromagnetic phase (martensite) was exploited to establish the relationship between the microstructural phases and magnetic properties of steel. It was found that dislocation pileups and misorientations in the structure significantly affect the overall saturation magnetization of the material. The derived relation between the saturated magnetization and the volume fractions of the retained austenite to martensite phases holds well for low-alloy high-carbon DP steels. The relationship can be extended to other grades of steel by broad-range benchmark methods, as employed in the study.

Copyright: 10.1002/adem.202300826
N. Sarmadi, F. Pahlevani, S. Udayakumar, *et al.*
Advanced Engineering Materials

References:

[1] Dutta, T. *et al*. (2019). Designing dual-phase steels with improved performance using ANN and GA in tandem. *Computational Materials Science*. DOI: 10.1016/j.commatsci.2018.10.020.

[2] Kalhor, A. *et al*. (2020). A review of recent progress in mechanical and corrosion properties of dual phase steels. *Archives of Civil and Mechanical Engineering*. DOI: 10.1007/s43452-020-00088-0.

[3] Das, D. and Chattopadhyay, P.P. (2009). Influence of martensite morphology on the work-hardening behavior of high strength ferrite–martensite dual-phase steel. *Journal of Materials Science*. DOI: 10.1007/s10853-009-3392-0.

[4] Lesch, C. *et al*. (2017). Advanced High Strength Steels (AHSS) for Automotive Applications – Tailored Properties by Smart Microstructural Adjustments. *steel research international*. DOI: 10.1002/srin.201700210.

[5] Mumtaz, K. *et al*. (2002). Use of saturation magnetism measurements to detect martensite formation in austenitic stainless steel after compressive deformation at high temperatures. *Journal of Materials Science Letters*. DOI: 10.1023/A:1016568402120.

[6] Vértesy, G. *et al*. (2024). Evaluation of the Embrittlement in Reactor Pressure-Vessel Steels Using a Hybrid Nondestructive Electromagnetic Testing and Evaluation Approach. *Materials*. DOI: 10.3390/ma17051106.

[7] Tavares, S.S.M. *et al*. (2006). X-ray diffraction and magnetic characterization of the retained austenite in a chromium alloyed high carbon steel. *Journal of Materials Science*. DOI: 10.1007/s10853-006-0025-8.

[8] Tamura, I. (1982). Deformation-induced martensitic transformation and transformation-induced plasticity in steels. *Metal Science*. DOI: 10.1179/030634582790427316.

[9] Sherby, O.D. *et al*. (2008). Revisiting the Structure of Martensite in Iron-Carbon Steels. *MATERIALS TRANSACTIONS*. DOI: 10.2320/MATERTRANS.MRA2007338.

[10] Hossain, R. *et al*. (2019). Stability of retained austenite in high carbon steel – Effect of post-tempering heat treatment. *Materials Characterization*. DOI: 10.1016/j.matchar.2019.01.034.

[11] Bida, G. V. *et al*. (2001). Magnetic properties of steels after quenching and tempering. I. General. Carbon steels. *Russian Journal of Nondestructive Testing*. DOI: 10.1023/A:1016767721717/METRICS.

[12] Zhao, L. *et al*. (2001). Magnetic and X-ray diffraction measurements for the determination of retained austenite in TRIP steels. *Materials Science and Engineering: A*. DOI: 10.1016/S0921-5093(01)00965-0.

[13] Babasafari, Z. *et al*. (2021). Effect of Microstructural Features on Magnetic Properties of High-Carbon Steel. Metallurgical and Materials Transactions A: *Physical Metallurgy and Materials Science*. DOI: 10.1007/S11661-021-06458-4/FIGURES/19.

Microstructure and Wear Behavior of the High-Velocity- Oxygen-Fuel Sprayed and Spark Plasma Sintered High-Entropy Alloy AlCrFeCoNi

Adapted from M. Löbel, *et al.*, 2020

In this study, high-entropy alloy AlCrFeCoNi powder is produced by inert gas atomization and then processed by high-velocity-oxygen-fuel thermal spraying. Alternative processing route and resulting material characteristics are explored for a better understanding of microstructural effects in high-entropy alloys.

Introduction

Recent research focuses on high-entropy alloys (HEAs), typically exhibiting high ductility but relatively low strength and hardness in a face centered cubic (fcc) structure [1]. Investigating additional alloying elements to stabilize a body centered cubic (bcc) structure has been explored [2,3]. Equimolar alloy AlCrFeCoNi achieves a single-phase bcc structure in its as-cast state [4,5] but undergoes phase formation and increased heterogeneity with subsequent heat treatment. Heat treatment at 850°C forms an additional σ-phase, causing embrittlement. Higher temperatures lead to σ-phase decomposition and the formation of an additional ductile fcc phase, resulting in advantageous mechanical properties, tested in a compression test [6].

Bulk alloys are produced via powder metallurgy, with spark plasma sintering (SPS) offering rapid production of dense alloys [7]. Typically, mechanically alloyed or atomized powder is used, and adjusting process parameters allows for control over phase contents and resulting mechanical properties. Coating technologies limit material usage to surfaces, with thermal spray processes, particularly high-velocity-oxygen-fuel (HVOF) spraying, being widely used in industry due to low thermal input [8]. Despite extensive studies on phase formation and mechanical properties of alloy AlCrFeCoNi, its impact on wear behavior remains underexplored. Hence, the current investigation scrutinizes the influence of microstructure and phase formation on wear behavior through varied production routes and heat treatments.

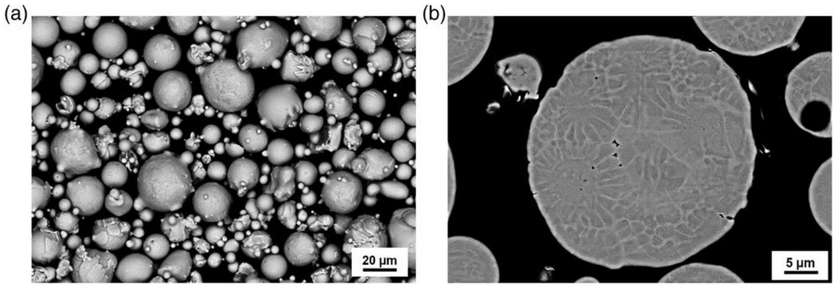

Figure 1. *Atomized AlCrFeCoNi powder investigated by SEM (SE/BSD): a) surface and b) cross section.*

Experimental Section

The equimolar alloy AlCrFeCoNi was atomized with argon. Then, the powder was classified to -45+15 µm (-d90+d10 µm). SEM LEO 1455VP (Zeiss, Jena) inspected cross sections and powder morphology, with a four-quadrant solid-state electron backscatter detector (BSD) for microstructure. Energy-dispersive X-ray spectroscopy (EDS) determined chemical composition, and X-ray diffraction (XRD) analyzed phase formation. Coatings were thermally sprayed onto stainless-steel substrates, and microstructure and phase formation were similarly investigated. Solution annealing occurred at 1050°C for 4 h, while SPS compacted feedstock powder. Microstructure and phase formation were examined via electron backscatter diffraction (EBSD) with SEM NEON 40 EsB (Zeiss, Jena). Microhardness (Vickers) was tested under various tribological conditions, including ball-on-disk tests for sliding wear and scratch tests for abrasive wear, all at room temperature.

Results and Discussion

The powder particles exhibit a predominantly spherical shape, as shown in the SEM (Figure 1a). This morphology is typical for gas-atomized powder. A BSD image of a metallographic cross section shows the dendritic solidification of the powder particles, but no distinct material contrast occurs (Figure 1b).

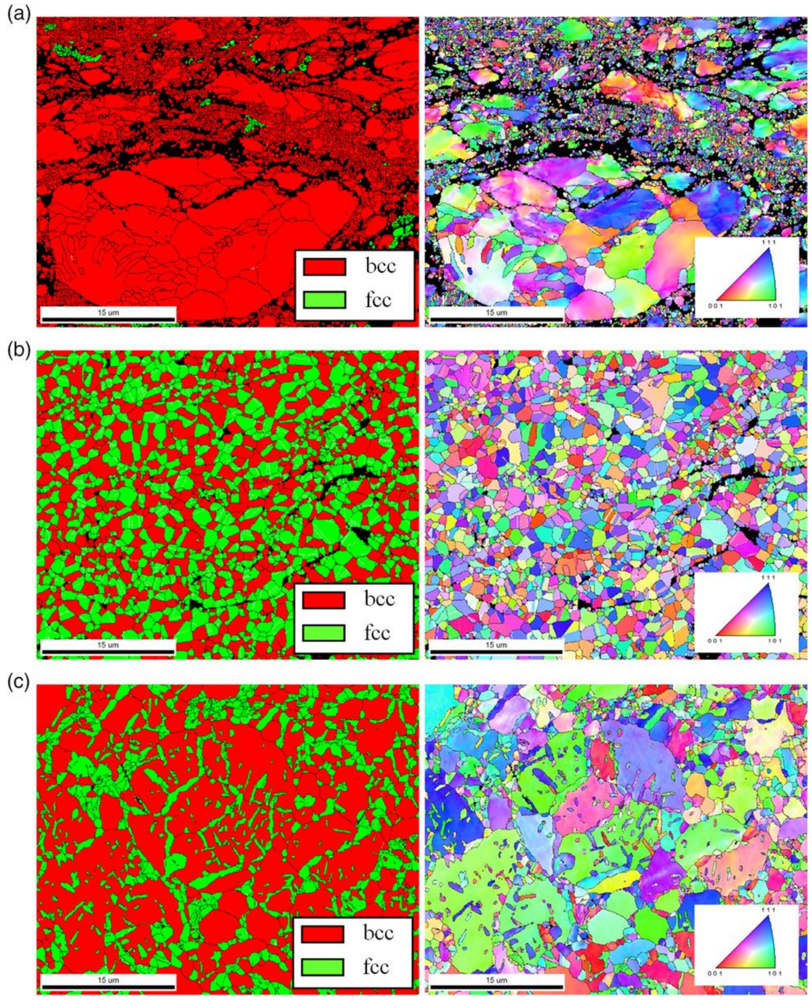

Figure 2. *Phase map with fcc phase in green and bcc phase in red (left) and orientation distribution with coloring according to the standard triangle (right) of the equimolar alloy AlCrFeCoNi: a) as-sprayed coating; b) solution annealed coating, and c) bulk alloy produced by SPS.*

In the as-sprayed state (Figure 2a), the coating exhibits a fine-grained lamellar structure, indicating thorough melting and quenching during thermal spraying. Some slightly deformed feedstock particles are visible incidentally. Not all areas could be indexed due to the presence of pores, cracks, and oxides, shown in black. Predominantly, a single bcc phase is formed, with a minor fraction of an fcc phase apparent. No distinct twin boundaries are observed in the coating.

Solution annealing (Figure 2b) led to a more uniform grain size distribution, eliminating the fine-grained lamellar structure present in the as-sprayed coating. Mainly equiaxed grains were formed, indicating recrystallization and grain size leveling. In addition to the primary bcc phase, a significant ≈51% fraction of an fcc phase emerged, exhibiting distinct twin boundaries typical of phases with low stacking-fault energy [9]. Similar twin boundary formation is observed in conventional alloys with an fcc structure, such as copper or austenitic steel, as well as HEAs with an fcc structure [10,11].

The powder metallurgically produced bulk alloy (Figure 2c) displays a distinct microstructure compared to the coatings in the as-sprayed and annealed states, appearing coarser. The shape of former feedstock particles is evident, indicating no melting during processing. Despite the rapid powder metallurgical processing via SPS, an additional fcc phase forms. The fcc phase content, approximately 32%, is lower than in the solution annealed coating, likely due to the lower thermal energy input during processing compared to annealing.

EDS point measurements showed that solution annealing increased aluminum and nickel content in the bcc phase, while chromium content decreased compared to the equimolar composition. Aluminum strongly stabilizes bcc phases [12,13]. In areas with an fcc structure, high chromium and iron content was found, with reduced aluminum and nickel content.

Chemical composition analyses of the powder metallurgically produced bulk alloy exhibited a similar trend. Phase composition depended notably on the production route, especially the temperature-time profile, altering diffusion behavior.

Microhardness measurements examined the effect of microstructure and phase formation on mechanical properties. The highest microhardness (600 ± 50 HV 0.1) was in the as-sprayed coating, showing a single-phase bcc structure. Solution annealing reduced microhardness to 390 ± 20 HV 0.1 due to the formation of a ductile fcc phase and reduced residual stress. The bulk alloy from SPS had slightly increased hardness (430 ± 10 HV 0.1) with the formation of an additional fcc phase, albeit at a lower fraction due to lower heat input. Structural defects like pores and oxide lamellae were absent, resulting in reduced hardness standard deviation compared to the solution annealed coating.

The as-sprayed coatings show the lowest wear resistance and reduced microhardness. Wear resistance increases in the solution annealed state due to the formation of an additional ductile fcc phase, albeit with a higher standard deviation attributed to heterogeneous states. The bulk alloy from SPS exhibits similar wear resistance, also with the formation of an additional ductile fcc phase but at a lower content. Compared to the solution annealed coating, reduced structural defects lead to decreased standard deviation. Reciprocating wear tests reveal a similar trend. In scratch tests under abrasive conditions, no distinct influence of the production route on wear behavior is observed.

Conclusions

Coatings of the equimolar alloy AlCrFeCoNi were produced via HVOF thermal spraying, resulting in a single-phase bcc structure. Solution annealing of the coatings reduced hardness compared to the as-sprayed state but notably improved wear resistance under sliding and reciprocating conditions, with no significant change observed under abrasive conditions. The bulk alloy produced by SPS exhibited the highest wear resistance due to the duplex structure formation and absence of structural defects like porosity and oxides. These findings suggest that wear resistance in HEAs can be enhanced through the formation of a duplex structure with ductile phases. Further studies on heat treatment parameters' effect on fcc phase content and resulting properties are warranted.

Copyright: 10.1002/adem.202001253
M. Löbel, T. Lindner, S. Clauß, *et al.*
Advanced Engineering Materials

References

[1] Gao, M. and Qiao, J. (2018). High-Entropy Alloys (HEAs). *Metals*. DOI: 10.3390/met8020108.

[2] Alaneme, K.K. *et al*. (2016). Processing, alloy composition and phase transition effect on the mechanical and corrosion *properties of high entropy alloys: a review. Journal of Materials Research and Technology*. DOI: 10.1016/J.JMRT.2016.03.004.

[3] Tsai, M.H. *et al*. (2017). Effect of atomic size difference on the type of major intermetallic phase in arc-melted CoCrFeNiX high-entropy alloys. Journal of Alloys and Compounds. DOI: 10.1016/J.JALLCOM.2016.10.286.

[4] Wang, F.J. *et al*. (2009). Cooling rate and size effect on the microstructure and mechanical properties of AlCoCrFeNi high entropy alloy. *Journal of Engineering Materials and Technology*. DOI: 10.1115/1.3120387/465369.

[5] Li, C. *et al*. (2010). Effect of aluminum contents on microstructure and properties of AlxCoCrFeNi alloys. *Journal of Alloys and Compounds*. DOI: 10.1016/J.JALLCOM.2010.03.111.

[6] Munitz, A. *et al*. (2016). Heat treatment impacts the micro-structure and mechanical properties of AlCoCrFeNi high entropy alloy. *Journal of Alloys and Compounds*. DOI: 10.1016/J.JALLCOM.2016.05.034.

[7] Olevsky, E.A. and Dudina, D. V. (2018). Field-assisted sintering: Science and applications. Field-Assisted Sintering: *Science and Applications*. DOI: 10.1007/978-3-319-76032-2/COVER.

[8] Oksa, M. *et al*. (2011). Optimization and Characterization of High Velocity Oxy-fuel Sprayed Coatings: *Techniques, Materials, and Applications*. Coatings. DOI: 10.3390/COATINGS1010017.

[9] Kopezky, Ch.V. *et al*. (1991). Multiple twinning and specific properties of $\Sigma = 3^n$ boundaries in f.c.c. crystals. *Acta Metallurgica et Materialia*. DOI: 10.1016/0956-7151(91)90248-Y.

[10] Geissler, D. *et al*. (2011). Appearance of dislocation-mediated and twinning-induced plasticity in an engineering-grade FeMnNiCr alloy. *Acta Materialia*. DOI: 10.1016/j.actamat.2011.08.040.

[11] Bahmanpour, H. *et al*. (2011). Effect of stacking fault energy on deformation behavior of cryo-rolled copper and copper alloys. *Materials Science and Engineering: A*. DOI: 10.1016/j.msea.2011.09.022.

[12] Tsai, M.H. and Yeh, J.W. (2014). High-Entropy Alloys: A Critical Review. *Materials Research Letters*. DOI: 10.1080/21663831.2014.912690.

[13] Lindner, T. *et al*. (2017). The Phase Composition and Microstructure of AlxCoCrFeNiTi Alloys for the Development of High-Entropy Alloy Systems. *Metals*. DOI: 10.3390/MET7050162.

Enhanced Structural Stability of Yttria-Stabilized Zirconia–$LaMgAl_{11}O_{19}$ Dual Ceramic Coating by an α-Al_2O_3 Layer

Adapted from H. Tao, *et al.*, 2024

A ceramic coating (AlY) was applied atop a thermal barrier coating (CoCrNiAlY–YSZ–$LaMgAl_{11}O_{19}$) to enhance its longevity and structural integrity. The potential oxidation damage mechanisms of coatings with and without the AlY layer were studied.

Introduction

Thermal barrier coatings (TBCs) are vital for safeguarding high-temperature components due to their oxidation resistance and low thermal conductivity [1,2]. Yttria-stabilized zirconia (YSZ) is commonly used, but its susceptibility to sintering and phase transformation can cause premature TBC failure [3]. To address this, double-layer TBCs with a ceramic surface layer and YSZ intermediate layer are gaining attention [4]. $LaMgAl_{11}O_{19}$ (LaMA) shows promise as a surface layer due to its thermal properties, but crystallization during processing can lead to micro-cracks [5].

Soleimanipour *et al*. [6] demonstrated the efficacy of an Al_2O_3 layer on YSZ, enhancing TBC lifespan. An AlY plating layer was applied onto a CoCrNiAlY–YSZ–LaMA dual-ceramic coating. The structural changes of the AlY layer during high-temperature exposure and its impact on oxidation behavior was then investigated.

Materials and Methods

The GH188 super-alloy substrates (15mm × 15mm × 5mm) underwent thorough oxide removal before coating. Corundum pellets (240 mesh) were then used for sandblasting. Employing Atmospheric Plasma Spraying (APS) technology, dual ceramic coatings of CoCrNiAlY–YSZ–LaMA were applied. The CoCrNiAlY powder comprises 31.0–34.0% Ni, 24.5–26.5% Cr, 5.0–6.5% Al, and 0.4–0.8% Y. An AlY layer, with 3 wt.% Y content in the target material and a 20 µm thickness, was deposited atop LaMA through arc ion plating.

The CoCrNiAlY powder consists of 31.0–34.0% Ni, 24.5–26.5% Cr, 5.0–6.5% Al, and 0.4–0.8% Y in wt.%, with Co making up the remainder. The YSZ powder comprises balanced ZrO_2 and 7.0–7.5 wt.% Y_2O_3. The LaMA powder contains 15.0–24.0% La_2O_3, 4.0–7.0% MgO, and balanced Al_2O_3 in wt.%. Morphologies of LaMA, YSZ, and CoCrNiAlY powders are depicted in Figure 1.

The oxidation behavior of all samples was assessed under air exposure conditions, with a heating rate of 10°C/min over 80 hours at 1000°C. Mass changes were monitored to analyze weight gain trends. Phase structure variations were investigated using X-ray diffraction (XRD), while surface and cross-sectional microstructures were examined via Scanning Electron Microscopy (SEM, Zeiss SIGMA HD). Surface interface elemental distribution of the coating was analyzed through Energy-dispersive spectroscopy (EDS).

Results and discussion

SEM images show sample Y1 (CoCrNiAlY–YSZ–LaMA) with a dense surface, typical of APS coatings, featuring visible holes and micro-cracks. The cross-sectional image reveals a clear three-layer structure of CoCrNiAlY, YSZ, and LaMA with strong interface bonding. Sample Y2 (CoCrNiAlY–YSZ–LaMA–AlY) exhibits a cauliflower-like surface, with the AlY layer effectively filling micro-cracks. EDS analysis confirms

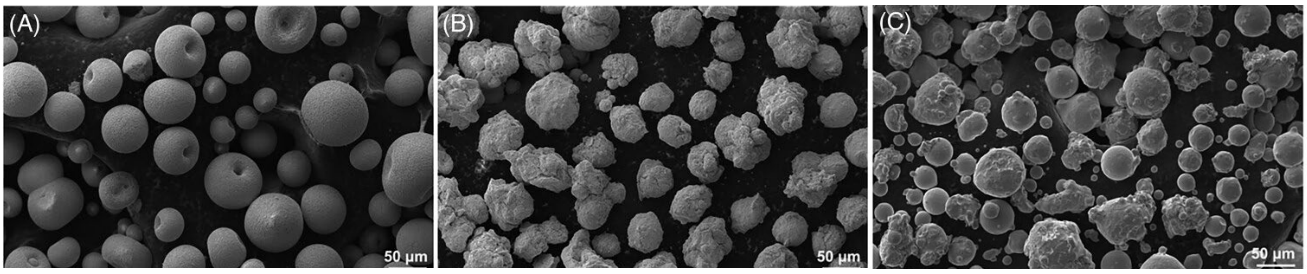

Figure 1. *Morphology of LaMA-YSZ, and CoCrNiAlY powders: (A) LaMA; (B) YSZ; (C) CoCrNiAlY.*

the presence and strong adhesion of the AlY layer on the LaMA.

During oxidation tests, Y2 demonstrates superior antioxidant performance compared to Y1, with a mass gain of 0.530 mg/cm^2 versus 4.017 mg/cm^2 for Y1. Y1 exhibits rapid weight gain over time, indicating increased oxidation, while Y2 initially experiences high mass gain due to AlY layer oxidation but later shows slower oxidation, suggesting improved resistance.

XRD analysis shows that Y1 is primarily composed of LaMA phases, with increasing intensity over time suggesting accelerated crystallization [7]. A small amount of $LaAlO_3$ phase is also detected. Y2 exhibits LaMA and $LaAlO_3$ phases, along with a significant presence of α-Al_2O_3 phase, indicating the formation of an in situ α-Al_2O_3 reaction film on the LaMA layer.

After 80 hours of oxidation testing, micro-cracks in LaMA up to 10.68 μm width can be seen. Longitudinal cracks extend further, leading to localized fracture in the YSZ bonding layer, and transverse penetration cracks form at the YSZ and CoCrNiAlY junction, indicating severe structural failure. In contrast, sample Y2 maintains a relatively dense surface, with only slight damage to the LaMA layer. Local α-Al_2O_3 formations are evident on the coating surface. Although a few transverse micro-cracks appear in the YSZ layer, overall, the coating structure exhibits stability with good interface adhesion. EDS elemental mapping confirms the formation of a continuous α-Al_2O_3 enrichment layer on the LaMA, effectively sealing micro-cracks induced by crystallization reactions.

Figure 2 displays SEM and EDS results of thermally grown oxide (TGO) layers in all coatings post 80-hour oxidation tests. Sample Y1 exhibits severe elemental diffusion, forming a composite TGO layer about 8 μm thick. The gray TGO layer (Region 1) shows high Cr (43.07 at.%) and O (21.29 at.%) contents, while the black TGO layer (Region 2) has high Al (40.42 at.%) and O (28.51 at.%) contents. Al_2O_3 constitutes the bottom black oxide layer [8], while $(Ni, Co)Cr_2O_4$ is mainly responsible for the gray oxide layer. Sample Y2 experiences slight elemental diffusion, with a thicker black TGO layer and a thinner gray TGO layer. Regions 3 and 4 confirm that the black and gray layers predominantly consist of Al_2O_3 and $(Ni, Co)Cr_2O_4$, respectively.

Sample Y1 shows poor high-temperature oxidation resistance, marked by severe elemental diffusion, rapid TGO growth, and interface fracture failure. This may result from oxidative degradation accelerating spinel phase formation and inducing higher growth stresses. Inherent defects like holes and micro-cracks in the sprayed coating facilitate oxygen diffusion during high-temperature oxidation. Additionally, recrystallization and volume shrinkage of the LaMA layer during high-temperature oxidation trigger the initiation of longitudinal micro-cracks [5], compromising the coating's barrier effect. Oxygen diffuses downward through these defects and large-scale longitudinal micro-cracks during the initial oxidation stage, reaching the CoCrNiAlY and YSZ interface.

Conclusions

The dual ceramic coating with an AlY plating layer showed improved oxidation resistance and structural stability during high temperature air exposure of plated CoCrNiAlY–YSZ–LaMA coating. A dense α-Al_2O_3 layer formed on the LaMA, which successfully blocks O_2 inward transport, as well as the quick development and high stress initiation of TGO layer, and eventually resulted in low mass gain and relatively stable structure.

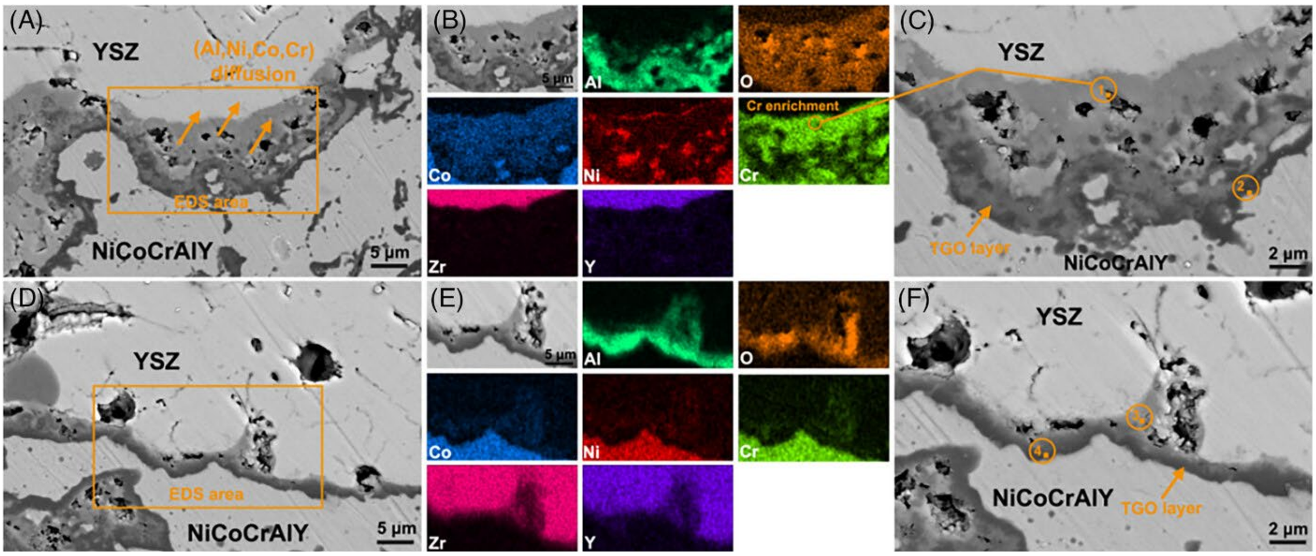

Figure 2. *SEM and EDS characterization results of TGO layer after 80 h oxidation: (A–C) Y1; (D–F) Y2.*

References

[1] Shen, Z. *et al*. (2021). Effects of Er stabilization on thermal property and failure behavior of Gd2Zr2O7 thermal barrier coatings. *Corrosion Science*. DOI: 10.1016/j.corsci.2021.109418.

[2] Doleker, K.M. *et al*. (2021). Oxidation and hot corrosion resistance of HVOF/EB-PVD thermal barrier coating system. Surface and Coatings Technology. DOI: 10.1016/j.surfcoat.2021.126862.

[3] Liu, Q. *et al*. (2019). Composite ceramics thermal barrier coatings of yttria stabilized zirconia for aero-engines. Journal of *Materials Science & Technology*. DOI: 10.1016/j.jmst.2019.08.003.

[4] Zhou, X. *et al*. (2020). Thermophysical properties and cyclic lifetime of plasma sprayed $SrAl_{12}O_{19}$ for thermal barrier coating applications. *Journal of the American Ceramic Society*. DOI: 10.1111/jace.17319.

[5] Huang, L. *et al*. (2014). Crystallization behavior of plasma-sprayed lanthanide magnesium hexaaluminate coatings. *International Journal of Minerals, Metallurgy, and Materials*. DOI: 10.1007/s12613-014-1034-2.

[6] Soleimanipour, Z. *et al*. (2016). Hot corrosion behavior of Al_2O_3 laser clad plasma sprayed YSZ thermal barrier coatings. *Ceramics International*. DOI: 10.1016/j.ceramint.2016.08.090.

[7] Xue, G. *et al*. (2021). Effect of Vacuum Annealing on Microstructure and Hot-Salt Corrosion Behavior of CoNiCrAlY/YSZ/$LaMgAl_{11}O_{19}$ Double-Ceramic Coating. *Coatings*. DOI: 10.3390/coatings11080951.

[8] Shi, J. *et al*. (2020). Isothermal oxidation and TGO growth behavior of NiCoCrAlY-YSZ thermal barrier coatings on a Ni-based superalloy. *Journal of Alloys and Compounds*. DOI: 10.1016/j.jallcom.2020.156093.

Effect of Mo Addition On Interfacial Microstructure And Mechanical Property Of SiC Joint Brazed By An Ni–Si Filler

Adapted from A. Kamal, *et al.*, 2024

This study explores the impact of Mo in Ni–30Si alloy on SiC brazing. Enhanced mechanical properties were observed with the addition of 8% Mo to the filler, attributed to microstructural changes within the grain.

Introduction

SiC ceramics are valued for high-temperature applications due to their low density, specific strength, corrosion resistance, and radiation tolerance [1]. Brazing is favored for SiC joining due to its simplicity, reliability, and reproducibility [2]. Ni-based alloy fillers, like Ni–28Mo, are commonly used for their superior performance at high temperatures and resistance to irradiation. However, notable cracks can occur in the bonded interphase due to differences in coefficient of thermal expansion (CTE) between Ni-based silicides and SiC substrate [3]. Maintaining a low graphite content ensures uniform Mo distribution, reducing residual stress, while excessive graphite compromises joint integrity [4]. The inclusion of Zr/Si in fillers enhances mechanical properties by eliminating graphite, but excessive Zr leads to brazing difficulties and reduced joint quality [5]. Si-rich fillers show promise in joint strength, but unreacted Si contributes to debonding at the Si–SiC interface at high temperatures, resulting in weak joints [6]. Considering molybdenum's higher melting point and lower CTE compared to other alloying elements, investigating its potential applications is worthwhile. In this study, Ni–30Si alloy powder was mixed with varying amounts of pure Mo powders for joining SiC ceramics.

Experimental procedure

SiC monoliths were fabricated via hot pressing of SiC (α-SiC). Composition of brazing filler was Ni–30Si with varying Mo concentrations (0, 4, 8, and 12 at.%), labeled as Mo-0, Mo-4, Mo-8, and Mo-12 respectively. Bonding was performed in vacuum at 1300 ± 10°C. The resulting SiC ceramic bonds were labeled J-Mo-0, J-Mo-4, J-Mo-8, and J-Mo-12, corresponding to the Mo-0, Mo-4, Mo-8, and Mo-12 filler formulations. The experiments included differential scanning calorimetry (DSC), measurement of elemental powder size, wetting and contact angle measurements, thermo-mechanical analysis for coefficient of thermal expansion (CTE), and lap shear strength (LSS) testing. Hot press epoxy mounted samples were polished to 1 µm grit finish to investigate the microstructure of the joint interface using a field emission SEM (FE-SEM) (Zeiss Supra 55) by employing the accelerating voltage up to 15 kV. The atomic composition of elements present was estimated by energy-dispersive X-ray spectroscopy (EDS). The phases were identified using X-Ray Diffraction (XRD). Thermodynamic calculations were performed using the Thermo-Calc program package.

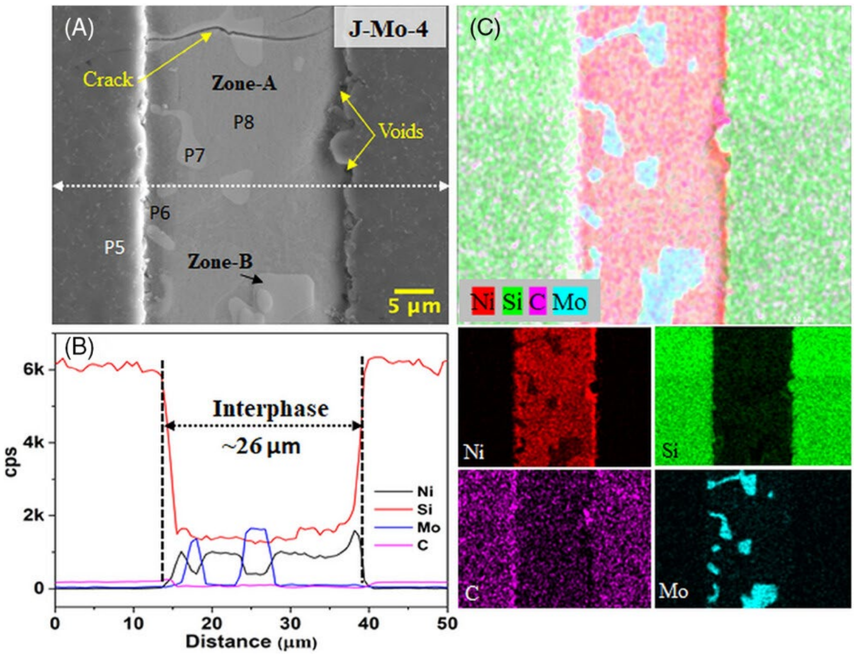

Figure 1. *(A) SEM images, (B) line scan and EDS mapping, and (C) elemental mapping of J-Mo-12.*

Results and discussion

Microstructural characterization of joints

The joint interface comprises a central reaction region and an interfacial reaction zone (IRZ). Ni and Si or Ni–Si-based compounds are evenly distributed in the central region, while Ni–Si-based compounds and graphite clusters form a dendritic structure in the IRZ. XRD analysis of J-Mo-0 identified δ-Ni_2Si, Ni_3Si_2, and graphite phases. Successful brazing with Ni–30Si alloy showed graphite and δ-Ni_2Si + Ni_3Si_2 phases in the IRZ, with the central zone dominated by δ-Ni_2Si. Incorporating 4% Mo into the Ni–30Si filler significantly reduced defects, with the interphase consisting mainly of a grey matrix and white flocculants, dominated by Ni–Si-based and Ni–Mo–C-based compounds, respectively. Mo_2C formation, reacting with local Ni to produce Ni_3Mo_3C, inhibited graphite presence, enhancing joint strength. Increasing Mo content to 8% yielded a defect-free joint with reduced CTE, maintaining a similar microstructure as the 4% Mo case. With 12% Mo, the interphase thickened significantly, subdivided into four zones (A, B, C, D), as can be seen in Figure 1. Despite a lower CTE, crack formation persisted due to thermal mismatch among Ni-rich, graphite, and Mo-rich phases. Nonetheless, the 8% Mo addition resulted in a defect-free joint with a consistent microstructure, highlighting the homogeneous distribution of Ni-rich and Mo-rich regions across the interface.

Mechanical performance of joints

The SiC joints, tested for lap shear strength (LSS) using Mo-containing Ni–30Si alloys, showed significant variations in performance. SEM-EDS analysis of the fractured surfaces (Figure 2) provided insights into morphology and composition at debonded sites. J-Mo-0 joint exhibited failure at 36 MPa due to various defects, whereas incorporating 4% Mo doubled the LSS to 72 MPa, with fracture at the SiC substrate indicating graphite absorption by Mo. Further increase in Mo content up to 12% resulted in decreased LSS to 75 MPa due to graphite-induced interface separation. Optimal joint strength was achieved with 8% Mo, showing enhanced microstructure and absence of graphite. The interface exhibited newly formed phases—δ-Ni_2Si, Ni_3Si_2, Mo_2C, and Ni_3Mo_3C—without graphite, showcasing robust SiC–SiC joints with excellent shear strength under pressureless brazing.

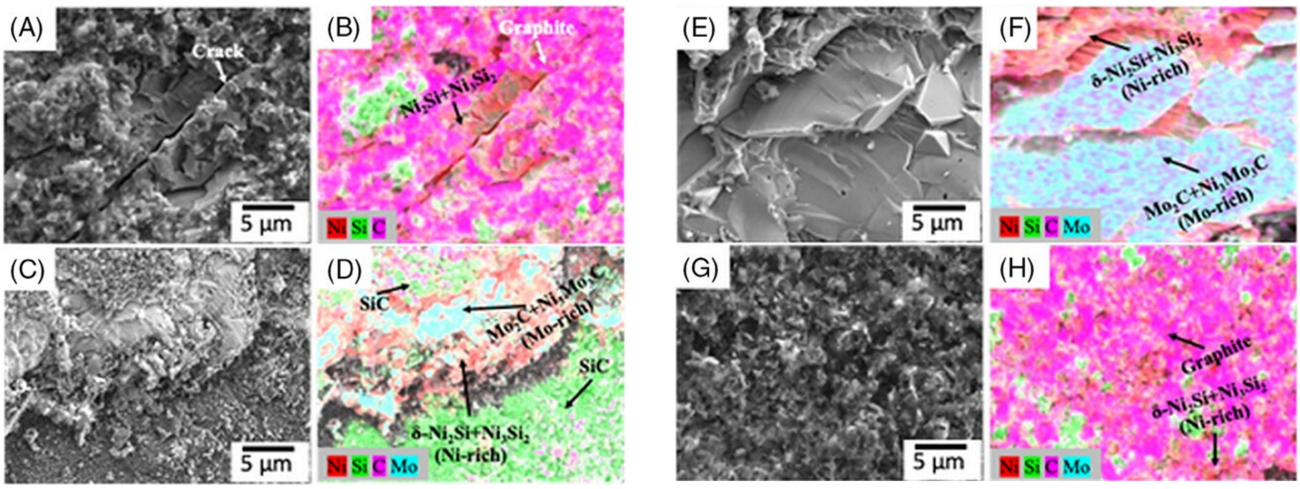

Figure 2. *SEM-EDS analysis for fracture surface of (A, B) J-Mo-0; (C, D) J-Mo-4; (E, F) J-Mo-8; and (G, H) J-Mo-12*

Joining mechanism

The process involves three stages: brazing, bonding, and testing. Figure 3A shows the joint made with 4% Mo (J-Mo-4), where Ni reacts with Si to form δ-Ni_2Si and Ni_3Si_2 phases concentrated at the central interface. Ni and Mo diffuse towards SiC, forming compounds like δ-Ni_2Si and Ni_3Si_2, and precipitating graphite particles. Mo reacts with graphite, forming Mo_2C, and further reacts with Ni to form Ni_3Mo_3C, visible as Mo-rich phases in Figure 3B. In J-Mo-8, Ni and Mo diffuse towards SiC, while Si and C diffuse towards the interphase (Figure 3D). The interphase thickens to ~40 µm, with distinct Ni-rich and Mo-rich regions (Figure 3E). Cracks observed during the LSS test (Figure 3F) propagate through the filler material.

In J-Mo-12 (Figure 3G), Ni diffuses towards SiC, forming δ- Ni_2Si and Ni_3Si_2, with carbon atoms liberating. These phases deposit as a Ni-rich layered structure at the interface. Carbon atoms migrate to the interlayer, transforming into Mo_2C. Mo_2C reacts with Ni, forming Ni_3Mo_3C phases, leading to coarsening and merging of Mo_2C/Ni_3Mo_3C grains, resulting in a 15-fold increase in Mo-rich phase area compared to J-Mo-4. Graphite acts as nucleation sites, sandwiched between Ni and Mo-rich phases. During cooling, stress concentration induces crack formation. The primary filler constituent is mostly Ni_3Si_2, and the Mo-concentrated region is primarily composed of Ni_3Mo_3C. The interphase thickness significantly increases to ~93 µm, attributed to the volume increase of newly formed phases.

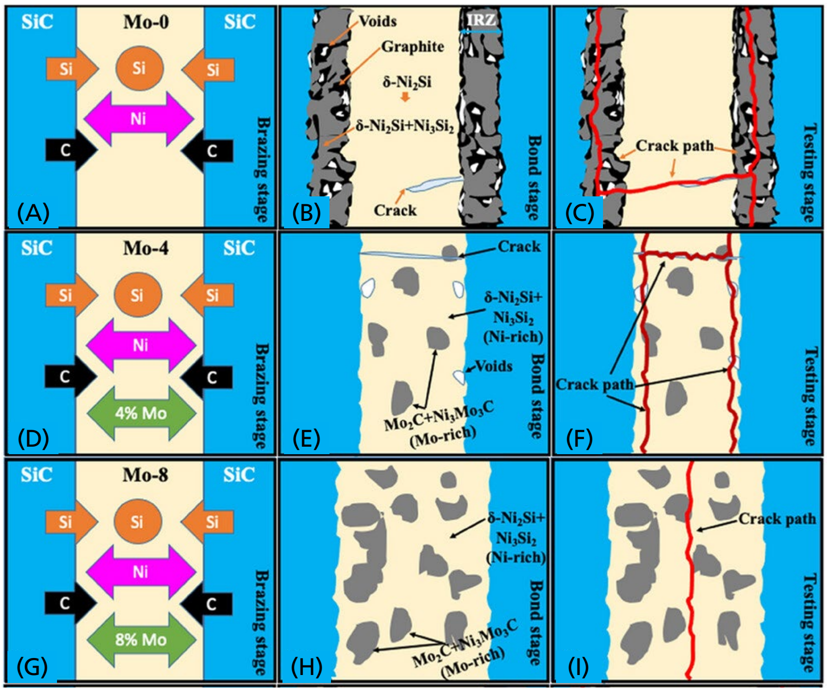

Figure 3. *Conceptual interfacial microstructural evolution model for J-Mo-4 (A, B, C); J-Mo-8 (D, E, F); and J-Mo-12 (G, H, I) for SiC–SiC joints.*

Conclusions

SiC ceramic was joined using Ni–30Si filler with varying Mo concentrations at 1300°C. At 8% Mo loading, the alloy achieved thermodynamic equilibrium with SiC, eliminating graphite at the interface. However, Mo loading exceeding 12% led to increased unit cell volume of reaction products, resulting in thicker interphase and non-uniform phase distribution, increasing residual graphite concentration and weakening joint strength. Incorporating 8% Mo into Ni–30Si yielded a high-quality SiC joint with evenly distributed newly formed high-temperature stable phases (Ni-based and Mo-based) near the contact region.

Copyright: 10.1111/jace.19677
A. Kamal, A. Kumar Shukla, V. M. Shinde, *et al*.
Journal of the American Ceramic Society

References

[1] Snead, L.L. *et al*. (2007). Handbook of SiC properties for fuel performance modeling. *Journal of Nuclear Materials*. DOI: 10.1016/j.jnucmat.2007.05.016.

[2] Sciti, D. *et al*. (2001). Bonding of zirconia to super alloy with the active brazing technique. *Journal of the European Ceramic Society*. DOI: 10.1016/S0955-2219(00)00162-X.

[3] Tian, W.B. *et al*. (2017). Brazing of silicon carbide ceramics with Ni-Si-Ti powder mixtures. *Journal of the Australian Ceramic Society*. DOI: 10.1007/s41779-017-0061-7.

[4] Wang, Z. *et al*. (2021). Joining of SiC ceramics using the Ni-Mo filler alloy for heat exchanger applications. *Journal of the European Ceramic Society*. DOI: 10.1016/j.jeurceramsoc.2021.07.056.

[5] Chen, D. *et al*. (2018). Incorporating Zr combined Si and C to achieve self-repairing ability and enhancement of silica sol bonded SiC castables. *Journal of Alloys and Compounds*. DOI: 10.1016/j.jallcom.2017.10.233.

[6] Yin, X. *et al*. (2010). Fabrication and characterization of a carbon fibre reinforced carbon–silicon carbide–titanium silicon carbide hybrid matrix composite. *Materials Science and Engineering: A*. DOI: 10.1016/j.msea.2009.08.069.

Evolution of Local Misorientations in the γ/γ'-Microstructure of Single Crystal Superalloys During Creep Studied with the Rotation Vector Baseline Ebsd Method

Adapted from S. Gamanov, *et al.*, 2023

The present work uses the rotation vector baseline electron back scatter orientation imaging method (RVB-EBSD) to study the evolution of small misorientations between the γ- and γ'-phase in Ni-base single crystal superalloys (SXs) during creep.

Introduction

Plastic deformation in metallic single crystals involves lattice rotations [1]. Large single crystal deformation via single slip can cause significant lattice rotations. This study characterizes rotation phenomena in high-temperature, low-stress [001] tensile creep of Ni-base single crystal superalloys (SXs). These alloys consist of ordered γ'-cubes (l12-phase, 75% volume fraction, average edge length 0.4 µm) separated by narrow γ-channels (FCC crystal structure, ~25% volume fraction, average width ~50 nm). During creep, dislocations form networks near γ/γ'-interfaces. Network spacings (s) characterize the misfit between γ- and γ'-phases [2,3], with misorientation angle (θ) related to s as $\theta=b/s$, b being the Burgers vector [4]. In SXs, dislocation networks develop early in creep. This study aims to explore microstructural evolution in early creep stages using orientation imaging scanning electron microscopy (OI-SEM), despite challenges like narrow γ-channels and indistinguishable Kikuchi line diffraction patterns of γ and γ' phases [5], as shown in Figure 1. In that context, chemical differences between phases are exploited [6]. The study upgrades the rotation vector baseline electron backscatter diffraction (RVB-EBSD) method [7] to resolve orientation differences of 0.03°. Optimized imaging parameters, virtual dark field technique, and enhanced post-processing algorithms [8,9] are employed to characterize γ/γ'-microstructure orientation features. Additionally, diffraction contrast scanning transmission electron microscopy (STEM) is used at selected interfaces.

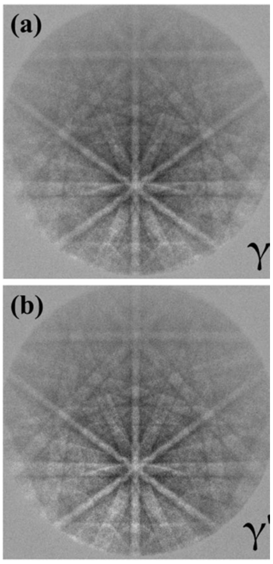

Figure 1. *Examples EBSD patterns obtained from the material state deformed to 1% from γ-region (a), and γ'-region (b).*

Experiments and methods

The alloy ERBO/1 (CMSX-4 type) was examined [6]. Miniature creep specimens were crafted with precise crystallographic orientations (<1° deviation). Two crept material states, deformed at 850°C under 600 MPa stress to strains of 1% and 2%, were analyzed.

For OI-SEM, high-quality (100) specimen surfaces were prepared through grinding, diamond paste polishing, and vibro-polishing. SEM analysis was conducted using a Zeiss Leo Gemini 1530VP equipped with an FEG, in-lens BSE detector, and an EBSD system from EDAX with Digiview Camera running TSL software. The RVB-EBSD method [7], facilitated high-resolution measurement of kernel average misorientations (KAM) angles and visualization of orientation spreads across larger specimen regions.

Standard EBSD indexation procedures proved insufficient for distinguishing between γ and γ'-phases, as depicted in the image quality map (Figure 2a). Contrast enhancement relied on exploiting slight differences in background illumination due to variations in chemical composition between the γ and γ'-phases [6]. Notably, dendritic regions of the γ-phase exhibited higher levels of Co, Cr, Re, and W (wt%: 17.8, 17.1, 12.7, and 10.1, respectively) compared to the γ'-phase (wt%: 5.9, 1.7, 0.7, and 6.1, respectively) [6].

Wright *et al.* demonstrated that the EBSD detector can be used as a virtual electron diode to generate chemical contrast by integrating electron signals in specific areas (Figure 2) [9]. These signals, composed of diffracted and scattered electrons, carry valuable chemical information. By dividing the detector area into virtual front scatter diodes, virtual dark field images can be produced, aiding phase separation better than standard quality images. This contrast method, as shown by Nolze *et al.*, effectively differentiates between γ and γ' phases in Ni-based superalloys, a technique utilized in this study [10].

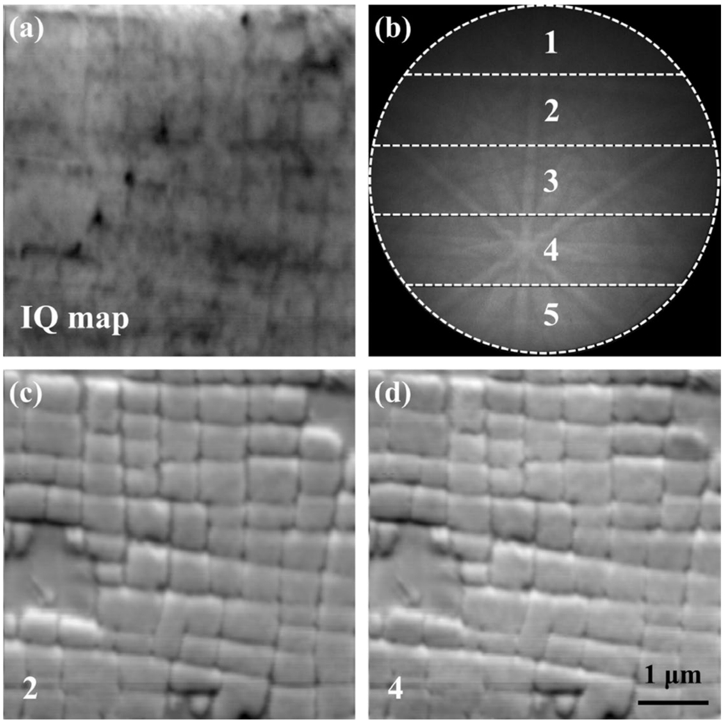

Figure 2. *EBSD results obtained using a step size of 20 nm. (a) Conventional image quality with poor phase contrast. (b) Subdivision of the detector area collecting the elastically and inelastically scattered electrons into 5 regions. (c) and (d) Virtual dark field images generated by signal integration over areas 2 and 4, respectively.*

Orientation information is obtained using the RVB-EBSD method, enabling KAM mapping for local misorientation assessment. A half-quadratic orientation filter enhances image quality, as evidenced by Figure 3a (without filter) and b (with filter). Although the signal-to-noise ratio improves, the input data's angular resolution may not unveil critical microstructural features and could introduce artifacts. Utilizing RVB-EBSD raw data initially ameliorates the situation, with further noise reduction achieved through filtering (Figure 3c,d). Subsequent EBSD investigations in this study rely on the combination of RVB-EBSD with half-quadratic filtering.

In early [001] tensile creep, dislocation plasticity primarily occurs in γ-channels perpendicular to stress [11]. Consequently, phase boundary misorientations (PBM) and KAM of γ-channels along perpendicular (⊥) and parallel (||) stress directions may differ systematically. To investigate, a separation technique for metallographic cross-sections is utilized. Rectangular windows are placed over regions with γ-channels, adjacent γ′ particles, and interfaces. PBMs and γ-channel KAM values are extracted and processed based on their assigned character (⊥ or ||). An algorithm identifies interface pixels inside each window, distinguishing between ⊥ and || interfaces. Manual adjustment ensures only straight interface portions are analyzed, excluding crooked segments and particle corners.

Results and discussion

KAM increase with creep strain, notably higher in γ-channels than in γ′ particles. A difference was calculated at a cumulative frequency of 0.5, rising from 27% at 1% creep to 39% at 2%. Perpendicular γ-channels exhibit slightly higher KAM values than parallel channels, a trend consistent even in the 2% deformed sample.

The RVB-EBSD technique resolves angular deviations from [100] orientation using relative pole figure color coding [7]. Crystallographic orientation spread extends beyond γ-channel and γ′-particle differences, encompassing larger-scale microstructural regions. These regions, comprising groups of γ′-particles larger than the average size (>0.5 μm) but smaller than dendrite spacing (<200 μm), exhibit slight misorientations to each other.

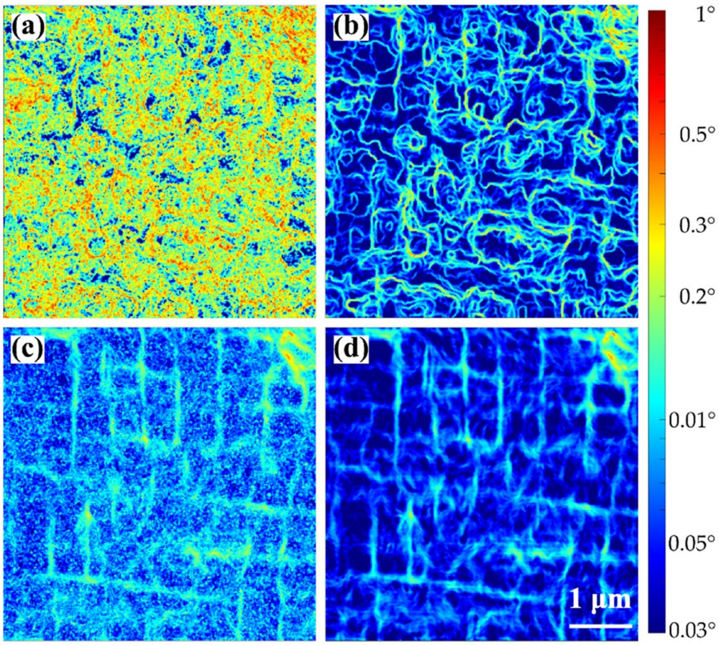

Figure 3. *Comparison of orientation results of KAM data. (a) Unfiltered data. (b) Filtered data. (c) Unfiltered rotation vector baseline electron backscatter OI method (RVB-EBSD) data. (d) Filtered RVB-EBSD data.*

An effective chemical contrast between γ and γ′ phases in single crystal superalloy CMSX-10 has been demonstrated [10]. The study confirms this method's applicability to CMSX-4, despite its weaker chemical contrast.

The early creep stages necessitate high-angular-resolution EBSD methods to capture evolving misorientations accurately. Kamaya *et al*. [12] proposed estimating EBSD map angular resolution by analyzing pixel neighborhoods at varying distances, yielding resolutions of 0.01° and 0.03° for 1% and 2% creep strains, respectively, aligning with Thome *et al.*'s simulated pattern shift results [7].

Dislocation loops entering γ′-channels during creep, depositing dislocations in γ-phase near γ/γ′-interfaces, exhibit a 60° character, contributing to an average spacing of 54 nm, consistent with literature [2]. Misorientations at γ/γ′-interfaces, associated with interface dislocation networks, average ≈ 0.25° after 2% creep.

PBM and KAM distributions for ⊥ and || γ-channels confirm early creep dislocation plasticity localization in ⊥ channels, with higher misorientation angles suggesting denser dislocation spacing. Overlapping distributions after 2% strain indicate a gradual balance between interfaces, though KAM distributions still favor ⊥ channels, hinting at slower dislocation recovery within. However, interpretations should consider small misorientation differences and limited statistics.

Conclusions

In this study, the RVB-EBSD method, initially designed for dendritic solidification analysis, is applied to track small misorientations in the γ/γ′ microstructures of a single crystal Ni-base superalloy during creep. Utilizing Kamaya's approach and cross-referencing with STEM data, RVB-EBSD demonstrates an angular resolution of 0.01 to 0.03° for specimens deformed to 1% and 2% strain under demanding experimental conditions.

Copyright: 10.1002/jemt.24453
S. Gamanov, A. Dlouhy, D. Bürger, *et al*.
Microscopy Research and Technique

References

[1] Schmid, E. and Boas, W. (1935). *Kristallplastizität Springer-Verlag*.

[2] Carroll, L.J. *et al*. (2008). Interfacial dislocation networks and creep in directional coarsened Ru-containing nickel-base single-crystal superalloys. Metallurgical and Materials Transactions A: *Physical Metallurgy and Materials Science*. DOI: 10.1007/S11661-008-9520-7/METRICS.

[3] Long, H. *et al*. (2017). A modification on Brook formula in calculating the misfit of Ni-based superalloys. Materials & Design. DOI: 10.1016/J.MATDES.2017.04.020.

[4] Hull, D. (1984). D. 1. BACON: Introduction to dislocations, 3rd edn, *International Series on Materials Science and Technology*, 246.

[5] Nishikawa, S. and Kikuchi, S. (1928). Diffraction of Cathode Rays by Mica. *Nature*. DOI: 10.1038/1211019a0.

[6] Parsa, A.B. *et al*. (2015). Advanced Scale Bridging Microstructure Analysis of Single Crystal Ni-Base Superalloys. *Advanced Engineering Materials*. DOI: 10.1002/ADEM.201400136.

[7] Thome, P. *et al*. (2019). Ni-base superalloy single crystal (SX) mosaicity characterized by the Rotation Vector Base Line Electron Back Scatter Diffraction (RVB-EBSD) method. *Ultramicroscopy*. DOI: 10.1016/J.ULTRAMIC.2019.112817.

[8] Hielscher, R. *et al*. (2019). Denoising of crystal orientation maps. *Journal of Applied Crystallography*. DOI: 10.1107/S1600576719009075.

[9] Wright, S.I. *et al*. (2015). Electron imaging with an EBSD detector. *Ultramicroscopy*. DOI: 10.1016/J.ULTRAMIC.2014.10.002.

[10] Nolze, G. *et al*. (2017). Electron backscatter diffraction beyond the mainstream. *Crystal Research and Technology*. DOI: 10.1002/CRAT.201600252.

[11] Wu, X. *et al*. (2016). Double minimum creep of single crystal Ni-base superalloys. *Acta Materialia*. DOI: 10.1016/J.ACTAMAT.2016.04.012.

[12] Kamaya, M. (2011). Assessment of local deformation using EBSD: Quantification of accuracy of measurement and definition of local gradient. *Ultramicroscopy*. DOI: 10.1016/J.ULTRAMIC.2011.02.004.

Advanced Microscopy Characterization of Metals and Alloys

An Interview with Kaoru Sato

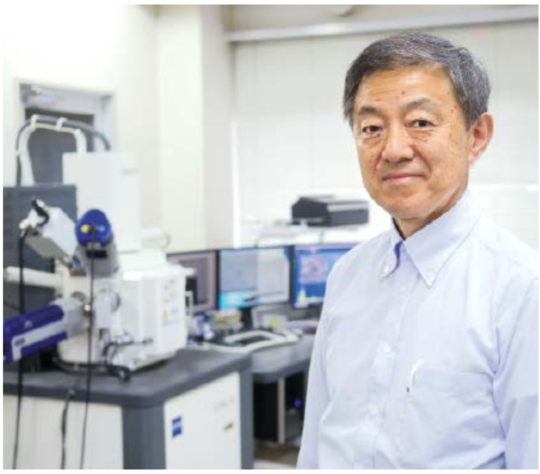

Kaoru Sato joined Nippon Kokan KK (NKK, predecessor of JFE Steel) in 1981. After he received a PhD from the University of Cambridge, UK, in 1989, he worked at JFE Steel as the General Manager of the Analysis & Characterisation Research Department. In 2011 he advanced to Principal Researcher at JFE Steel Corporation. From 2016 onwards, he has worked as a fellow of JFE-TEC, specializing in electron microscopy and microbeam analysis of material/surface design. He is also actively engaged in advanced analysis using synchrotron radiation and neutrons.

Here Dr Sato draws on his years of experience to share with us his views on current key issues in metal and alloy analysis, together with his expectations for the future.

Dr Sato-San, it seems like there is a strong momentum in the field of traditional metals and alloys, with research interest picking up both in academia and industry. Can you share your view about the driver for such a strong push?

When I give a talk on metals/steel to non-experts, I often quote Sir Alan Cottrell's remark:[1]

"Above all, there remains the continuing challenge of steel. For many reasons - an abundance of rich and reducible ores, high intrinsic strength and melting point, ease of alloying and richness of phase transformation behaviour - steel remains by far the best source of cheap, reliable tensile strength, and is unlikely ever to be overtaken in this 'mass-market' role."

It's encouraging that scientists are studying so called nano-tech materials such as carbon-nanotubes or cellulose nanofibres however it is unlikely that these materials will be used to a large degree in, for example, automobile production for several more decades. Demands for metal and steel are huge: developing countries need more steel. Not only the quantity but also the quality is vital. An article on Tokyo Skytree[2] highlights how the development of steel contributed to construction of this piece of modern architecture.

Limited amounts of rare metals and precious metals are available, and new alloy designs are vital to minimize the use of those metals for heat-resistant metals, magnets and catalysts.

In your opinion, what are the burning issues within the metals and alloys that are being addressed by academic and industrial researchers?

Our understanding of metals and alloys is still limited and the scope for future study is vast. Recent investigations suggest a new deformation mechanism for magnesium alloys. High-entropy alloys are of high interest among academia. We need an in-depth knowledge to make various materials with minimum addition of rare metals or precious metals. The role of H, B and C in steel is yet to be studied.

What do you consider as the significant milestones in the development of imaging technology for materials characterization that have and will continue to impact traditional metals research?

Imaging sciences have seen great advancement in this last half a century. Bright pri-

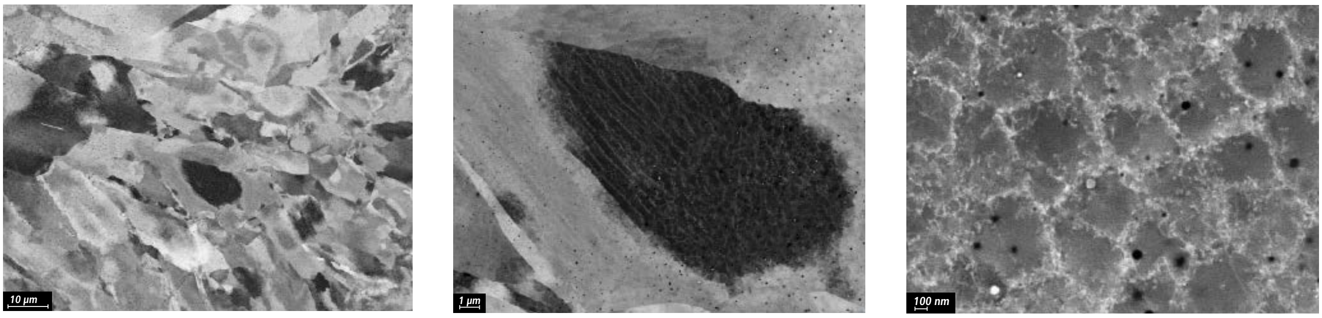

See the wood and the trees: Application to additive manufactured 316L stainless steel. Electron channelling contrast image (ECCI) reveals inhomogeneous strain distributions at low (left) and medium (centre) magnifications. Dislocation cell structures are discerned at high magnification (right).

mary beams, such as filed-emission gun and synchrotron sources, are routinely used today. Aberration correction in TEM and beam-deceleration optics, together with in-lens image detection in SEM, have dramatically improved the power of electron microscopy. We have strengthened our knowledge of atomic, interface and surface microstructures. Enhancements in light elements such as H, Li, B and C detection, detection and visualization of low-concentration elements in alloys, 3D imaging and *in situ* capabilities will give additional value to electron microscopy.

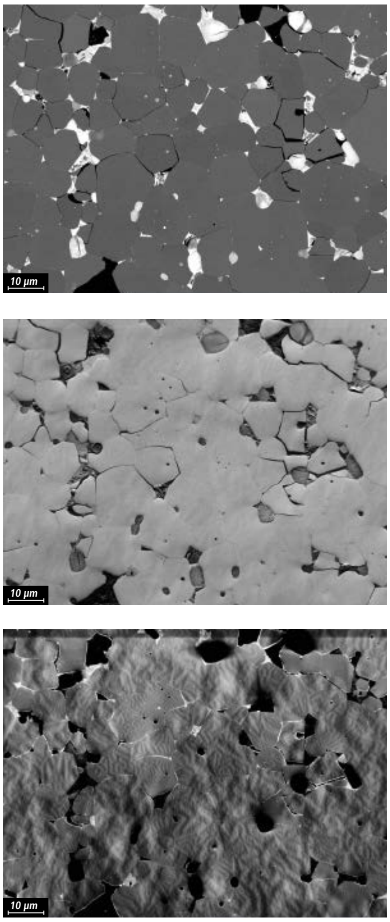

Power of multiple detectors: Application to Fe-Nd-B magnet. In-lens backscattered electron, E-T and In-lens secondary electron detectors give compositional, topographic and magnetic contrast, respectively (from top to bottom).

What are the benefits of your research with regard to the engineering materials supply of the future? What visions do you have for this?

My motto is "What cannot be seen or measured cannot be controlled", and this appears on the JFE-TEC webpage. I have a strong belief in observational science. Unless you understand or measure, you are not able to control. Let me emphasize that "It is not easy to find something in the total darkness, Microscopy is like light."

SEM is truly a powerful method. It allows observations from below x100 to above x100,000, thus you can see the wood and the trees, which is very important for engineering materials. We have been promoting imaging at the "sweet spot". In this context the ZEISS Gemini column was an eye-opener. This innovative instrument is giving new insights into understanding microstructure by providing unique image contrasts.

Through use of enhanced imaging and the analytical capabilities that I mentioned in the previous section, we will be able to contribute to sustainable development goals (SDGs) by designing alloys with minimum environmental loads.

You work extensively with electron microscopy and microbeam analysis. What advantages does this method offer you in your work and which areas of application have not yet exhausted the potential of this technology in your opinion?

Materials properties (e.g. mechanical and electrical properties) are governed by microstructure. Consequently, chemical bulk analysis alone cannot elucidate properties. A variety of methods using electrons, X-rays and neutrons can be successfully applied to the understanding of both hard and soft materials.

JFE-TEC work with many clients in the field of heat-resistant alloys, batteries, magnets and catalysts in order to achieve SDGs.

Atomic-level characterizations have become routine and they are contributing to material design. However, our challenges continue: we want to see atoms in motion, how materials break or corrode, and how the structure changes at elevated temperatures.

What has been your most important insight into metals and advanced materials technology to date, where modern imaging methods have served you well?

We have succeeded in developing novel steel products, including high-strength and high-formability steel and excellent press-formability surface coatings. Both TEM and SEM have played a crucial role in this development. It is indeed the nanostructure that governs properties. We are proud that we can stably produce nanostructure-controlled steel products in large volumes.

JFE-TEC have been promoting imaging at the "sweet spot". Apart from topographic information, SEM can give richer information provided you optimize the signal detection. This technique gives true surface information and a quick-and-handy assessment of precipitates in heat-resistant alloys.

What expectations do you have of equipment and software development with regard to the further improvement of microscopic analyses in your research area?

In situ/operando observation for both dry and wet specimens should be strengthened. Light elements and minor elements detection are another issue. To achieve this goal, further integration of the microscope and analytical instruments/*in situ* attachment will be crucial. Microscope manufacturers and analytical instruments companies should work more closely together in order to optimize their instruments.

Today we are dealing with more and more data: Giga-sized image acquisition has become routine, and we cannot inspect such huge data manually. AI or machine learning and implementation of automatic data inspection are strongly required.

Further integration of microscopes and analytical instruments will come. This will improve, for example, the detectability of low-concentration elements. Automated image acquisition and inspection of high-precision micrographs will be realized. Stored images will be archived and utilized as large databases.

References

[1] Pettifor DG, Cottrell A. Electron Theory in Alloy Design. Institute of Materials, 1992. ISBN 10: 0901716170, ISBN 13: 9780901716170

[2] Bringing neutrons into industry. Physics World, October 2017. https://physicsworld.com/a/bringing-neutrons-into-the-steel-industry/

JFE-TEC Gemini team in Kawasaki.


ZEISS
Gemini 2
GeminiSEM 460

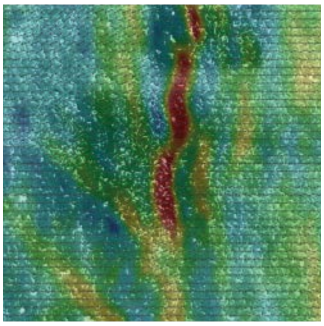


ZEISS
Gemini 2
Crossbeam 550